# Updraft Vertical Velocity Observations and Uncertainties in High Plains Supercells Using Radiosondes and Radars

PETER J. MARINESCU,[a] PATRICK C. KENNEDY,[a] MICHAEL M. BELL,[a] ARYEH J. DRAGER,[a] LEAH D. GRANT,[a] SEAN W. FREEMAN,[a] AND SUSAN C. VAN DEN HEEVER[a]

[a] *Department of Atmospheric Science, Colorado State University, Fort Collins, Colorado*

(Manuscript received 28 February 2020, in final form 14 July 2020)

ABSTRACT: Observations of the air vertical velocities ($w_{air}$) in supercell updrafts are presented, including uncertainty estimates, from radiosonde GPS measurements in two supercells. These in situ observations were collected during the Colorado State University Convective Cloud Outflows and Updrafts Experiment ($C^3$LOUD-Ex) in moderately unstable environments in Colorado and Wyoming. Based on the radiosonde accelerations, instances when the radiosonde balloon likely bursts within the updraft are determined, and adjustments are made to account for the subsequent reduction in radiosonde buoyancy. Before and after these adjustments, the maximum estimated $w_{air}$ values are 36.2 and 49.9 m s$^{-1}$, respectively. Radar data are used to contextualize the in situ observations and suggest that most of the radiosonde observations were located several kilometers away from the most intense vertical motions. Therefore, the radiosonde-based $w_{air}$ values presented likely underestimate the maximum values within these storms due to these sampling biases, as well as the impacts from hydrometeors, which are not accounted for. When possible, radiosonde-based $w_{air}$ values were compared to estimates from dual-Doppler methods and from parcel theory. When the radiosondes observed their highest $w_{air}$ values, dual-Doppler methods generally produced 15–20 m s$^{-1}$ lower $w_{air}$ for the same location, which could be related to the differences in the observing systems' resolutions. In situ observations within supercell updrafts, which have been limited in recent decades, can be used to improve our understanding and modeling of storm dynamics. This study provides new in situ observations, as well as methods and lessons that could be applied to future field campaigns.

KEYWORDS: Convective clouds; Updrafts/downdrafts; Vertical motion; Convective storms; Radars/Radar observations; Radiosonde observations

## 1. Introduction

Supercell updrafts contain some of the most intense vertical air velocities ($w_{air}$) in the atmosphere (e.g., Musil et al. 1986; Lehmiller et al. 2001; DiGangi et al. 2016). The magnitude and vertical structure of $w_{air}$ within supercell updrafts control many atmospheric processes, including the production of severe hail (e.g., Browning and Foote 1976; Heymsfield and Musil 1982) and the transport of atmospheric constituents from the boundary layer to the upper troposphere and stratosphere (e.g., Foote and Fankhauser 1973; Mullendore et al. 2005). Due to the strong vertical velocities in supercell updrafts, cloud droplets do not have enough time to grow to sizes that can be observed by most radars. Supercell updrafts can therefore be clearly identified in radar data as regions with lower reflectivity in the lower- and middle-tropospheric levels, laterally and vertically bounded by higher reflectivity, known initially as vaults and later as weak-echo regions or bounded weak-echo regions (WERs or BWERs; Browning and Ludlam 1962; Chisholm 1970; Marwitz and Berry 1971; Chisholm 1973). Despite supercell updrafts' importance for atmospheric processes, these updrafts have seldom been observed in situ.

The first of these infrequent in situ observations of the magnitudes of supercell updraft velocities came from armored aircraft penetrations through the WERs (Marwitz and Berry 1971; Heymsfield and Musil 1982). These observations were usually made near cloud base and in the inflow air ahead of the supercell and were typically taken in the High Plains of the United States and Canada. These initial in situ observations generally resulted in estimates of $w_{air}$ in the 15–30 m s$^{-1}$ range. One research flight into the WER of a supercell in Montana at ~7 km above mean sea level (MSL) observed $w_{air}$ as high as $50 \pm 5$ m s$^{-1}$ (Musil et al. 1986). Despite the continued need for in situ observations of deep convection, the last U.S. storm-penetrating research aircraft was retired without replacement in 2005 (Geerts et al. 2018).

In situ estimates of updraft velocities can also be achieved via releasing sensors or trackable objects into supercell updrafts from the storm's proximity. Chaff packets have been released from aircraft at thunderstorms' cloud bases and tracked with radar to estimate vertical velocities within supercells. Results from this approach have generally been consistent with those from in situ aircraft penetrations (Marwitz 1972, 1973). Radiosondes have also been used throughout the past 50 years, albeit infrequently, to estimate the vertical velocities in supercells (Barnes 1970; Davies-Jones 1974; Davies-Jones and Henderson 1975; Bluestein et al. 1988, 1989; Marshall et al. 1995; Markowski et al. 2018). From these radiosonde observations, the greatest reported $w_{air}$ values were 49 m s$^{-1}$ (Bluestein et al. 1988) and 53 m s$^{-1}$ (Markowski et al. 2018), which occurred in Texas and Oklahoma, respectively.

Due to the challenges associated with in situ observations of updrafts, such as the hazardous sampling conditions and the difficulty of placing sensors directly within the updraft core, remotely sensed observations have replaced in situ observations as

*Corresponding author*: Peter J. Marinescu, peter.marinescu@colostate.edu

DOI: 10.1175/MWR-D-20-0071.1

the primary estimates of $w_{air}$ in deep convection in recent decades. The most common method for estimating $w_{air}$ with remote sensing utilizes data from multiple Doppler radars to determine the horizontal components of the wind, and then invokes the mass continuity equation to calculate the vertical component of the wind (e.g., Armijo 1969; Miller 1975; Kropfli and Miller 1976; Gal-Chen 1978). Multi-Doppler retrievals can provide vertical velocities over a relatively large domain and are often conveniently gridded to Cartesian coordinates. However, multi-Doppler estimates also have hard-to-characterize uncertainties due to their sensitivities to analysis specifications, such as how the data are filtered or interpolated (e.g., Nelson and Brown 1987; Miller and Fredrick 1998; Collis et al. 2010; Shapiro et al. 2010) or the temporal and spatial resolution of the data (e.g., Bousquet et al. 2008; Potvin et al. 2012; Oue et al. 2019; Dahl et al. 2019). Because of their availability, these remotely sensed observations have often been used to validate case study model simulations of deep convection in large field campaigns (Varble et al. 2014; Marinescu et al. 2016; Fan et al. 2017). These studies have shown that cloud-resolving models tend to produce stronger vertical velocities than their corresponding radar-derived estimates. However, the errors associated with multi-Doppler $w_{air}$ are largely case-specific and depend on the radar scanning strategy, the type of convection and location of convection with respect to the radars (Oue et al. 2019). Therefore, it is still challenging to attribute the differences in updraft magnitudes from radar-based analyses and cloud-resolving models. In situ observations can thus assist in providing independent estimates of $w_{air}$.

In this study, we present GPS-radiosonde-based in situ observations and uncertainties of $w_{air}$ within the updraft regions of two supercells. These observations were made during the Colorado State University Convective Cloud Outflows and Updrafts Experiment ($C^3$LOUD-Ex) during 2016 and 2017 in the High Plains of Colorado, Wyoming, and Nebraska (van den Heever et al. 2020, manuscript submitted to *Bull. Amer. Meteor. Soc.*). Using the radiosonde data, along with radar observations within the $C^3$LOUD-Ex domain, we 1) provide our best in situ estimates of $w_{air}$ within the two supercell updrafts, 2) contextualize and compare these observations to other available $w_{air}$ estimates for the two cases, and 3) offer insights for future efforts toward obtaining in situ observations within supercell updrafts.

## 2. $C^3$LOUD-ex observations

### a. Radiosondes

During $C^3$LOUD-Ex, the iMet-1-ABxn radiosonde was used, which included a pressure, temperature, and humidity sensor, as well as a GPS receiver (InterMet Systems 2016). The radiosonde package was attached via a dereeler (30-m length) to a 200-g balloon that was filled with enough helium to reduce the helium tank's gauge pressure by approximately 3447 kPa (500 psi). For this study, the most essential radiosonde data were from the GPS receiver, which has a horizontal position accuracy of 10 m and an altitude accuracy of 15 m. GPS positions were received from the radiosonde at a rate of approximately 1 Hz and linearly interpolated to create a 1-Hz record.

Using the GPS altitude data, the vertical velocity of the radiosonde was estimated every second using a centered-in-time derivative:

$$w_{sonde} = \frac{\Delta z}{\Delta t}, \tag{1}$$

where $w_{sonde}$ is the representative vertical velocity of the radiosonde system over the time interval $\Delta t$, and $\Delta z$ is the vertical distance traveled by the radiosonde during $\Delta t$. For this study, $\Delta t$ is chosen to be 12 s, which for 10–60 m s$^{-1}$ updrafts equates to vertical distances of 120–720 m, comparable to current numerical model simulation grid spacings and/or observational grids. This $\Delta t$ is chosen in order to reduce the periodic signals that were present in this dataset on the time scales of 12 s and less, as described in more detail in appendix A. These periodic signals were likely associated with pendulum motions, which are theoretically estimated to have periods between 11 and 12 s for a dereeler length of 30 m. The periodic signals could also be associated with other self-induced balloon motions (e.g., Wang et al. 2009; Söder et al. 2019) that can occur on these small time scales. The error in this $w_{sonde}$, denoted $\epsilon_{w,sonde}$, was calculated using error propagation methods (e.g., Palmer 1912). Because the relative error in the GPS time measurement was several orders of magnitude smaller than the error in GPS position measurement $\epsilon_{w,GPS}$ can be simplified to the following:

$$\epsilon_{w,sonde} = |w_{sonde}|\left(\frac{\sqrt{2}\epsilon_z}{\Delta z}\right), \tag{2}$$

where $\epsilon_z$ is the error in the GPS altitude from the radiosonde (15 m). For a fixed $\Delta t = 12$ s and due to the linear relationship between $w_{sonde}$ and $\Delta z$, $\epsilon_{w,sonde}$ is always $\pm 1.8$ m s$^{-1}$. For the cases presented in this study, each increase of 2 s in $\Delta t$, for $\Delta t$ between 8 and 16 s, reduces the maximum vertical velocity observed by on average 0.1–0.5 m s$^{-1}$ due to smoothing and decreases the uncertainty by $\pm$0.1–0.4 m s$^{-1}$. Therefore, the results are minimally impacted by the choice of $\Delta t$.

While $w_{sonde}$ was directly observed by the radiosonde, the vertical velocity of the air that the radiosonde sampled ($w_{air}$) was desired. We decompose $w_{sonde}$ into the following components:

$$w_{sonde} = w_{air} + w_{buoy} + w_{upd\text{-}drag} + w_{upd\text{-}hydro}, \tag{3}$$

where $w_{buoy}$ is the vertical velocity arising from the buoyancy of the radiosonde system (balloon and radiosonde) in clear-sky, still-air conditions; $w_{upd\text{-}drag}$ is the vertical velocity associated with changes to the drag force on the radiosonde system within an updraft as compared to clear, still air; and $w_{upd\text{-}hydro}$ is the forcing from hydrometeors impacting or accumulating on the radiosonde system. Ultimately, by observing $w_{sonde}$, whose uncertainty ($\epsilon_{w,sonde}$) is known, and estimating $w_{buoy}$, $w_{upd\text{-}drag}$, $w_{upd\text{-}hydro}$, and their associated uncertainties ($\epsilon_{w,buoy}$, $\epsilon_{w,upd\text{-}drag}$, $\epsilon_{w,upd\text{-}hydro}$), an estimate of $w_{air}$ and its uncertainty ($\epsilon_{w,air}$) can be determined.

Implicit in these definitions is that in clear-sky, still-air conditions $w_{air}$, $w_{upd\text{-}drag}$, and $w_{upd\text{-}hydro}$ are all $\sim$0 m s$^{-1}$ and hence, $w_{sonde} = w_{buoy}$. Therefore, we estimated $w_{buoy}$ from the $w_{sonde}$

measurements obtained from thirteen radiosondes that were launched at the Colorado State University Foothills Campus in clear conditions with weak vertical motions throughout the troposphere. These radiosondes were launched during synoptic-scale ridges, which provided weak subsidence throughout the region. Seven launches took place overnight to minimize the influence of boundary layer vertical motions, as well as to eliminate the impacts of solar radiation on the balloon, which could affect the buoyancy of the radiosonde system (Farley 2005). Vertical profiles of $w_{buoy}$ for the clear-sky, still-air launches are shown in Fig. 1a. The radiosonde descent rates (red), which occur after the radiosondes' balloons burst, vary with altitude and have a greater spread than the ascent rates (blue), which are approximately constant throughout the troposphere and lower stratosphere. Figure 1b shows a normalized histogram of the ascent rates from the rising radiosondes. The mean upward vertical velocity from these experiments is 4.8 m s$^{-1}$ ($w_{buoy}$), with 90% of the data falling within ±1.1 m s$^{-1}$, which we define here as $\epsilon_{w,buoy}$. We also estimated the $w_{buoy}$ following the theoretical basis from Wang et al. (2009) and using a height-invariant drag coefficient of 0.5 for seven clear-air launches in which the free-lift weights were directly measured prior to launch. The theoretical $w_{buoy}$ varied with height, increasing from ~4.1–4.8 m s$^{-1}$ near the surface to ~5.0–6.0 m s$^{-1}$ at ~13 km MSL. These theoretical values overlap with the height-invariant estimate of $w_{buoy}$ obtained from observed $w_{sonde}$ from the clear-air launches (4.8 ± 1.1 m s$^{-1}$).

It is unknown whether and how the drag force on the radiosonde system within supercell updrafts differs from that in clear air, and we therefore assume that the $w_{upd\text{-}drag}$ is 0 m s$^{-1}$ (i.e., no systematic shifts in the radiosonde-based $w_{air}$ due to different drag forces within the updraft). Using the relationship between terminal velocity and the drag coefficient, however, we estimate that the uncertainty associated with variable drag forces on the radiosonde system within updraft conditions ($\epsilon_{w,upd\text{-}drag}$) is ±1.6 m s$^{-1}$ (see appendix B).

The forcing from hydrometeor impacts ($w_{upd\text{-}hydro}$) will typically be downward and can be caused by collisions with or accumulation of condensate mass (e.g., riming) on the radiosonde system. Because of the uncertainties in quantifying the presence and magnitude of these processes from the data available during C$^3$LOUD-Ex, we did not attempt to estimate $w_{upd\text{-}hydro}$ or its uncertainty in this study. Therefore, the radiosonde $w_{air}$ is expected to be most accurate in scenarios where there is little to no impact from hydrometeors on the radiosonde system (i.e., outside of regions with hydrometeors). In such situations, the radiosonde $w_{air}$ has an uncertainty ($\epsilon_{w,air}$) of ±2.6 m s$^{-1}$, where $\epsilon_{w,air}$ is the summation in quadrature of $\epsilon_{w,sonde}$ (±1.8 m s$^{-1}$), $\epsilon_{w,buoy}$ (±1.1 m s$^{-1}$), and $\epsilon_{w,upd\text{-}drag}$ (±1.6 m s$^{-1}$), following error propagation methods. In regions with hydrometeors, such as the cloudy regions of the supercell updraft, however, since $w_{upd\text{-}hydro}$ is negative for a rising balloon, the radiosonde $w_{air}$ represents a lower bound on the actual $w_{air}$. It is important to note here that these estimates also assume that the balloon has not burst. Using the radiosonde accelerations and the radar observations (as described in section 4), we estimated the times at which the balloons burst and made corresponding adjustments for those situations to provide a more realistic estimate of $w_{air}$.

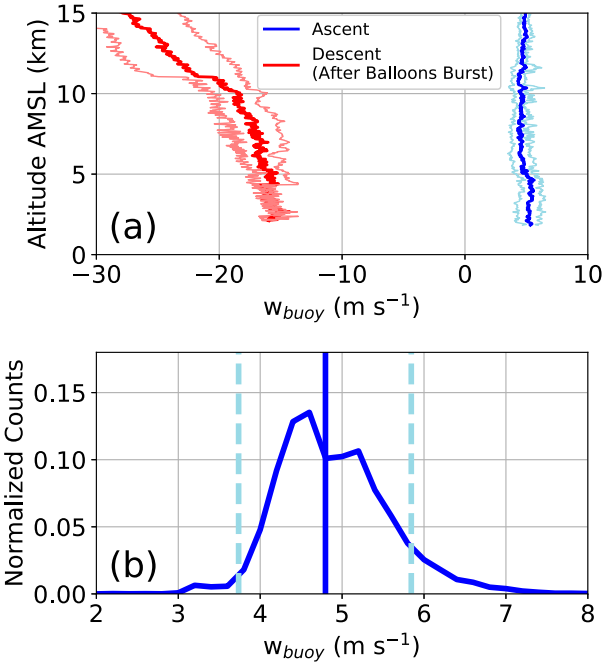


FIG. 1. (a) Mean $w_{buoy}$ during the clear still-air launches from ascending radiosondes (blue) and from descending radiosondes, after the balloons burst (red). Light blue and red lines represent one standard deviation from the mean. Data are not available for most descending radiosondes below 4.5 km MSL. (b) Normalized histogram counts from all $w_{buoy}$ from ascending radiosondes shown in (a), with the vertical solid line representing the mean value (4.8 m s$^{-1}$) and dashed lines representing ±1.1 m s$^{-1}$ from the mean, between which 90% of the data falls. The bin width is 0.2 m s$^{-1}$.

### b. Radars

Because the radiosondes provided localized measurements within the broad supercell updrafts, we used radar data to contextualize the in situ observations. Additionally, the radar data provided an independent estimate of $w_{air}$ using dual-Doppler methods. Three radars were primarily utilized during C$^3$LOUD-Ex: the CSU–CHILL radar (Brunkow et al. 2000), located in Greeley, Colorado; the Cheyenne, Wyoming NEXRAD (KCYS); and the Denver, Colorado NEXRAD (KFTG). KCYS is located ~79 km to the north of CSU–CHILL, and CSU–CHILL is located ~74 km to the north of KFTG. Plan position indicator (PPI) scans from all radars, as well as additional range height indicator (RHI) scans from CSU–CHILL, provided detailed views of the storm structure and the relative position of the radiosonde within the storms. During C$^3$LOUD-Ex, the NEXRAD radars (KCYS and KFTG) had prescribed volume coverage patterns (VCP212) that each lasted ~5 min, while the CSU–CHILL radar was manually operated and synchronized with the relevant NEXRAD radar during updraft-targeted radiosonde launches. Figure 2 shows an example of radar elevation angles for the NEXRAD and

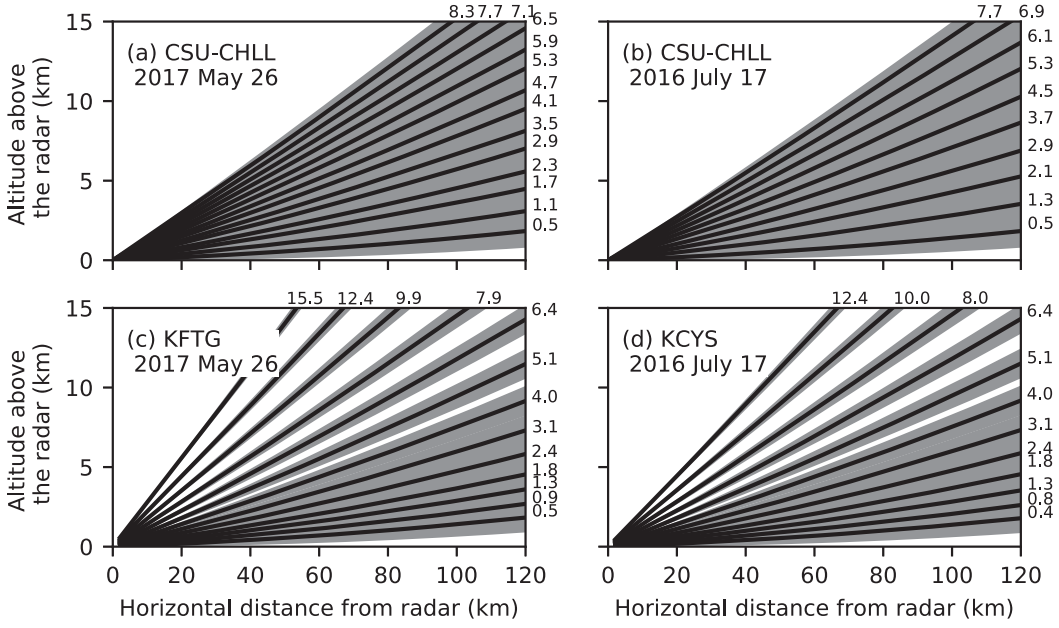


FIG. 2. Radar elevation angles for both the (a),(b) CSU–CHILL and (c),(d) NEXRAD radars during dual-Doppler analysis times for the two C$^3$LOUD-Ex cases. Black lines represent the center of the beams, while gray shading represents the vertical distance covered by the beams. The smaller numbers outside the panels represent the mean elevation angle used for the PPI scan.

CSU–CHILL radars for one radar volume for the two cases examined in this study.

Reflectivity, velocity, and some dual-polarization data from all three radars were used. These radar data were first quality-controlled using the dual-polarization data. Specifically, we excluded all radar gates where the standard deviation of the differential propagation phase was greater than 21° over a range of 11 gates. We found that this threshold eliminated noise and ground clutter, while retaining more data near features of interest (e.g., the WER), which were otherwise eliminated when using correlation coefficient as a threshold. The radar velocity data were dealiased using the region-based method in the Python-ARM Radar Toolkit (Py-ART; Helmus and Collis 2016), and the storm motion for both cases was estimated for each 5-min radar volume scan using the Py-ART grid displacement algorithm on the radar reflectivity between 3 and 8 km AGL. These estimated storm motions were calculated for each radar volume and used for corrections related to storm translation in the dual-Doppler analyses, as well as for advecting the radar analyses in time for comparisons with the 1-Hz radiosonde data. Although these processing steps were largely automated, all quality-controlled and processed data were also manually checked.

Two analysis programs were then used to synthesize the radial velocity data and produce radar-based $w_{\text{air}}$ estimates. These programs were the Custom Editing and Display of Reduced Information in Cartesian space (CEDRIC; Miller and Fredrick 1998) and the Spline Analysis at Mesoscale Utilizing Radar and Aircraft Instrumentation (SAMURAI; Bell et al. 2012). While these programs both solve the basic radar equations, CEDRIC uses column-by-column vertical integration of the mass continuity equation to produce local solutions for each vertical column, while SAMURAI uses a 3D-variational approach (Gao et al. 1999) and produces a global solution for the entire analysis domain via a cost minimization function. The 3D-variational approach has been shown to produce better vertical velocity solutions for a supercell case than other methods (Potvin et al. 2012). These analyses were completed on 1-km and 500-m Cartesian grids for the 26 May 2017 and 17 July 2016 cases, respectively, due to the relative locations of each storm with respect to the radars as shown in the following section. The top boundaries in the analyses were set to 17 km MSL (5–6 km above the tropopause) and the vertical velocities were set to 0 at the top boundary in SAMURAI and at half a vertical grid level above the highest level where divergence was calculated in each column in CEDRIC. For the CEDRIC analyses shown here, the variational vertical integration method was used, whereby downward integration was first completed, residual errors were spread throughout the column in an iterative manner and last, variationally adjusted integration was applied (e.g., $W_{\text{var}}$ in Dolan and Rutledge 2010). A linear, least squares two-dimensional filter was also used on the horizontal winds in the CEDRIC analyses (Miller and Fredrick 1998). Low-pass filters with approximate scales of 4 and 2 km for the 1-km and 500-m Cartesian grids, respectively, were applied in the SAMURAI analyses (Ooyama 2002, Purser et al. 2003).

## 3. C$^3$LOUD-ex cases

During C$^3$LOUD-Ex, there were seven cases in which the updrafts of supercell storms were successfully sampled with radiosondes (van den Heever et al. 2020, manuscript submitted

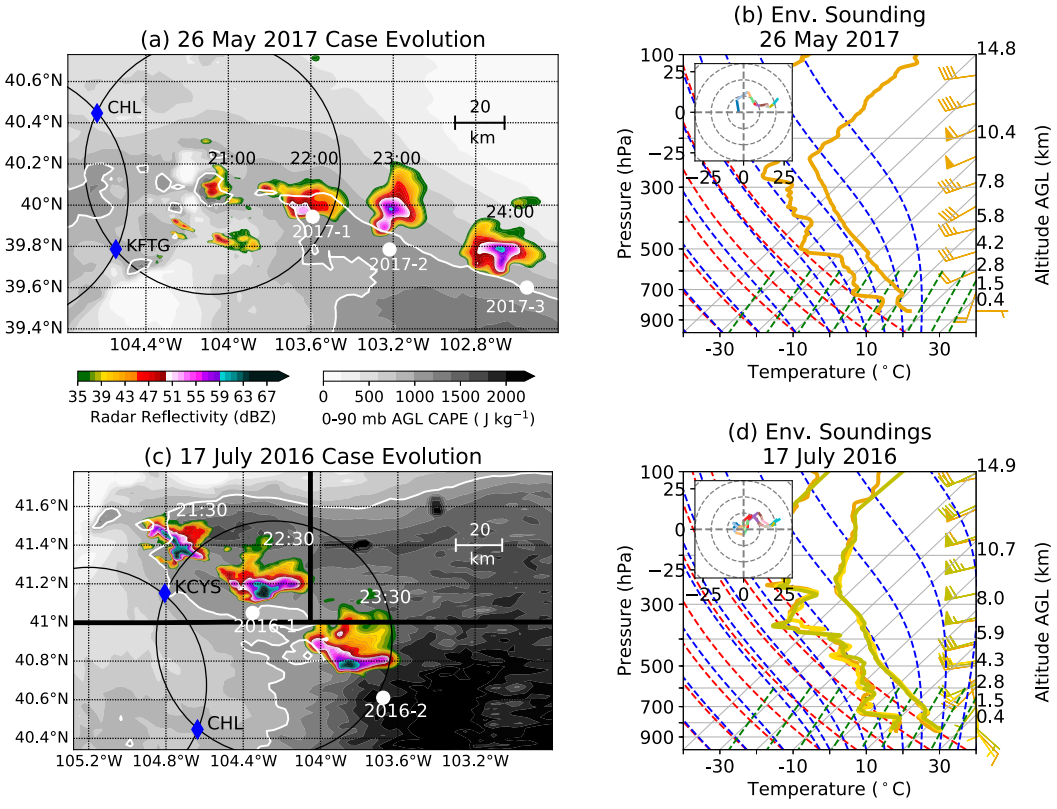


FIG. 3. (a),(c) Case evolution and (b),(d) environmental soundings from the (a),(b) 2017 case and (c),(d) 2016 case. The white dots represent the locations where the updraft radiosondes were launched. The blue diamonds are the radar locations, and nonoverlapping regions of the black circles indicate where dual-Doppler analyses are possible. The color shading shows radar reflectivity at 1 km AGL at the approximate time of radiosonde launch, gridded and interpolated from the available radars. The gray shading represents MLCAPE from the 2100 UTC operational simulation of High-Resolution Rapid Refresh (HRRR) model for both cases; 1000 J kg$^{-1}$ is contoured in white. The skew $T$–log$p$ diagrams of the environmental radiosonde launches in (b) and (d) are described in the text. Hodographs (m s$^{-1}$) are inlaid and the different colors within the hodographs represent 500-m increases in altitude from the surface to 6 km AGL.

to *Bull. Amer. Meteor. Soc.*). In this study, we focus on the two cases that had successful radiosonde sampling of updrafts within the regions where dual-Doppler estimates of $w_{air}$ could also be made. These occurred on 26 May 2017 and 17 July 2016 and are briefly described in the following two sections and summarized in Fig. 3.

### *a. 26 May 2017 case study*

At 1815 UTC (UTC = local time + 6 h), an environmental sounding (Fig. 3b) was launched at 39.72°N, 104.22°W and showed 0–6-km shear of 26 m s$^{-1}$, mixed-layer (0–90 hPa AGL) convective available potential energy (MLCAPE) of 491 J kg$^{-1}$, and surface-based CAPE of 1882 J kg$^{-1}$.[1] By 2000 UTC, terrain-induced scattered convection was moving eastward over the Denver metropolitan region. The destabilized boundary layer and favorable environmental conditions resulted in the development of an isolated supercell by 2200 UTC, located within the dual-Doppler analysis region for the CSU–CHILL and KFTG radars (Fig. 3a). At 2158 UTC, a radiosonde (2017-1) was launched and sampled the updraft of the developing supercell, while 1.5 in. (3.8 cm) diameter hail was reported at the surface nearby (NCEI 2017). Around 2200 UTC, the storm propagation slowed and took a rightward turn toward the east-southeast. Over the next several hours, many instances of hail with diameters of 1–1.5 in. (2.5–3.8 cm) were reported at the ground along the storm's path, as were 2 weak tornadoes (NCEI 2017). Two additional radiosondes (2017-2 and 2017-3) sampled the supercell updraft between 2200 and 2400 UTC. This long-lived supercell continued into Kansas, outside of the C$^3$LOUD-Ex domain, and subsequently became part of a mesoscale convective system.

### *b. 17 July 2016 case study*

On 17 July 2016 at ~2030 UTC, convection that had initiated over the high terrain of southern Wyoming moved eastward onto the high plains to the northwest of Cheyenne, Wyoming,

[1] The CAPE calculations in this study are based on Bryan (2008).

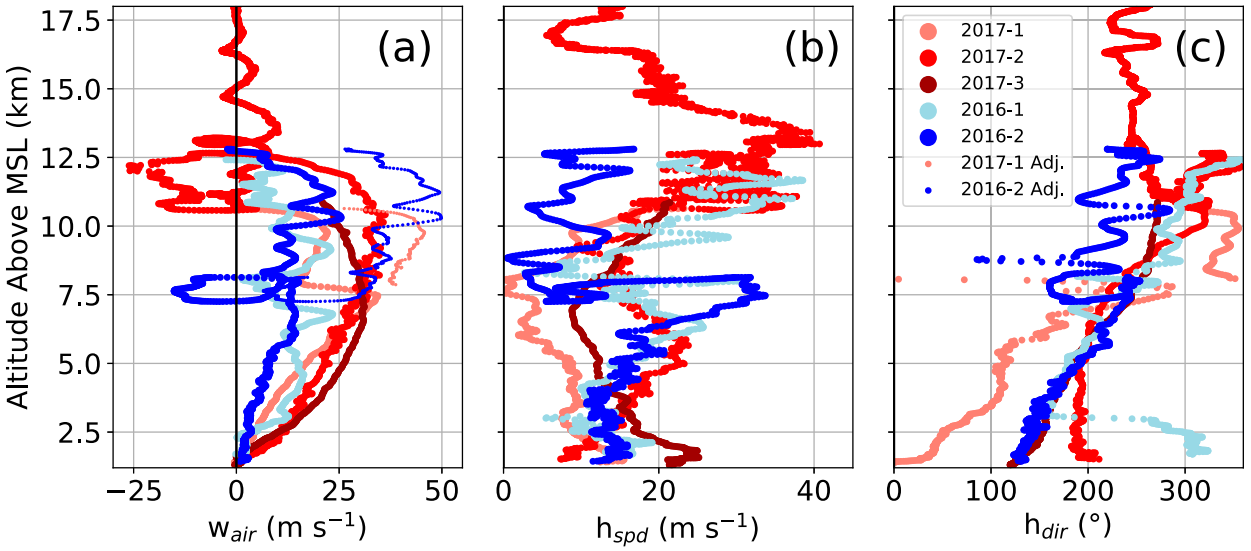


FIG. 4. (a) Radiosonde $w_{air}$ from radiosondes that sampled the two C$^3$LOUD-Ex supercell updrafts. (b),(c) The radiosondes' horizontal wind speed ($h_{spd}$) and horizontal wind direction ($h_{dir}$), respectively. In (c), 180° represents winds coming from the south. Data are only shown from the radiosondes' launch times through to when the radiosondes reached their maximum altitudes. The smaller dots for 2017-1 and 2016-2 represent $w_{air}$ adjusted for the assumption of a burst radiosonde balloon (see Fig. 5). Radiosonde data in this figure and subsequent figures are shown at 1-Hz frequency.

where it quickly organized into a supercell and subsequently turned toward the southeast (Fig. 3c). Earlier in the day, between 1800 and 1900 UTC, three radiosondes were launched (at 40.67°N, 104.33°W; 41.22°N, 104.35°W; and 41.24°N, 103.70°W) to better capture the environment ahead of this storm. These observations (Fig. 3d) indicate MLCAPE of ~950–1200 J kg$^{-1}$ and 0–6-km shear of 21–25 m s$^{-1}$. This supercell propagated southeastward across the C$^3$LOUD-Ex domain, including through the region where dual-Doppler analyses could be conducted using the CSU–CHILL and KCYS radars. This storm had more intense radar reflectivity than did the 2017 case, and there were several reports of 2.0-in. (5.1-cm) diameter hail as well as a few baseball-sized hailstones (diameters of ~7.5 cm; NCEI 2016). As the supercell propagated southeastward, two radiosondes were launched into the supercell's main updraft region (Fig. 3c). The first, 2016-1, was located within the dual-Doppler analysis region, while the second, 2016-2, was just outside the dual-Doppler lobes in a more unstable environment. By 0130 UTC 18 July 2016, the storm began to lose many of its supercellular characteristics, and it dissipated by 0300 UTC.

We note here that both of these High Plains supercells experienced environments with substantial vertical wind shear (0–6 km; ~21–26 m s$^{-1}$) and moderate MLCAPE (~1000–1600 J kg$^{-1}$). These environments had bulk Richardson numbers of ~10–15, well within the range favorable for supercells (Weisman and Klemp 1982), although the MLCAPE values are on the lower end of those conditions supporting weakly tornadic and nontornadic supercells within the broader United States (Thompson et al. 2003). Therefore, these C$^3$LOUD-Ex observations of $w_{air}$ will likely be lower than similar observations of supercells in more unstable air masses, such as those present in the U.S. southern Great Plains.

## 4. Radiosonde-derived updraft $w_{air}$

The $w_{air}$ estimated from the five radiosondes that sampled the two supercells' updrafts are shown in Fig. 4, which for simplicity's sake only depicts $w_{air}$ from when the radiosonde was launched to when the radiosonde reached its maximum altitude. The horizontal wind speed and direction were also calculated from the raw GPS data every second, using the same $\Delta t$ of 12 s. These radiosonde data represent point locations within the large supercell updrafts. Despite the radar's inability to observe the finer-scale motions observed by the radiosondes, the radar data were useful for determining the position of the radiosonde within the updraft and elucidating whether each radiosonde was in the vicinity of the strongest $w_{air}$ within these storms. The radiosondes took many different trajectories throughout the supercells. Only one of these five radiosondes (2017–2) continued to rise into the stratosphere after sampling the supercell updraft. The other radiosonde systems likely experienced conditions within the updraft that robbed them of their positive buoyancy (e.g., radiosonde balloon bursting or significant riming). To identify these events, the radiosonde-derived accelerations were calculated from the difference in the 1-Hz $w_{air}$ data and were examined for the entirety of the radiosondes' data transmissions (Fig. 5). A 5-s moving average was applied to the calculated acceleration to eliminate noise but still capture significant events. The most intense negative accelerations were assumed to be associated with the radiosonde balloon bursting, whereby $w_{buoy}$ instantaneously changed from approximately +4.8 m s$^{-1}$ to anywhere between −15 and −25 m s$^{-1}$, depending on the radiosonde's

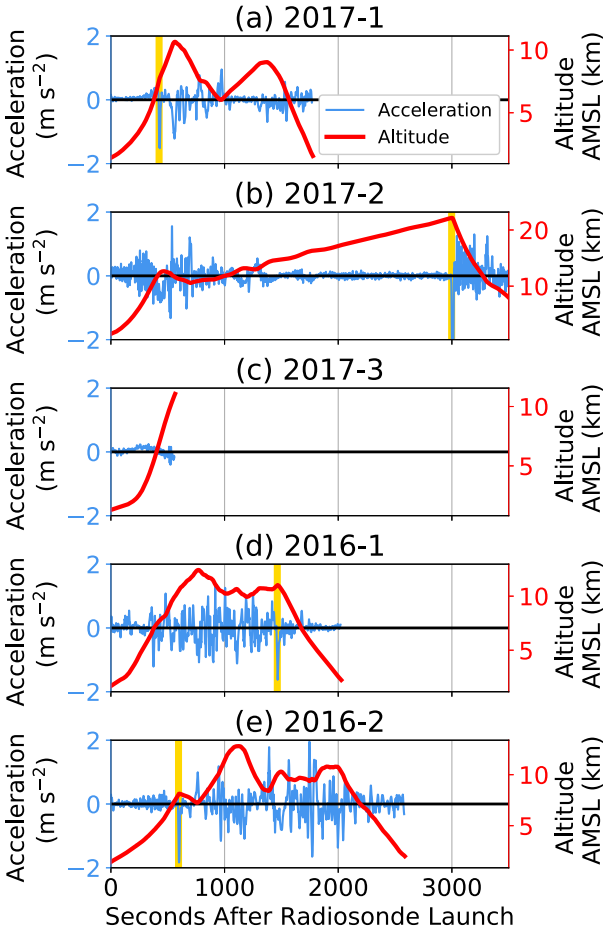


FIG. 5. Radiosonde accelerations from each launch (blue, left axis) and radiosonde altitude (red, right axis) as a function of seconds since launch. Yellow vertical lines indicate the strongest negative accelerations, which were assumed to be coincident with the radiosonde balloon bursting.

tropospheric altitude (Fig. 1a). It is possible that such intense negative accelerations could also be a result of significant icing and hydrometeor collisions with the balloon, although these effects are unquantifiable in our dataset. The most intense negative accelerations are highlighted in yellow in Fig. 5 and had values between $-1.4$ and $-4.3\,\mathrm{m\,s^{-2}}$. These values were similar to those associated with the radiosonde balloon bursts during the clear-sky, still-air launches, which all occurred above 16 km MSL and ranged from $-2.2$ to $-4.8\,\mathrm{m\,s^{-2}}$ (not shown). For radiosondes 2017-2 and 2016-1, the radiosondes' balloons did not burst until right before their final descents to the surface. However, for radiosondes 2017-1 and 2016-2, it appears that the balloon burst within the radiosonde's initial ascent through the updraft, based on the assumption that the most negative accelerations represent balloon bursts. While the likelihood of this relationship has yet to be established, radar data (shown in the following sections) suggest that the radiosondes 2017-1 and 2016-2 were entering regions of large hail within intense updrafts during their most negative accelerations, conditions that can cause a radiosonde balloon to burst. If the balloons had not burst, we would have expected these radiosondes to eventually exit the storm and rise into the stratosphere. Therefore, for radiosondes 2017-1 and 2016-2, adjustments were made to the radiosonde-derived $w_{\mathrm{air}}$ after the assumed balloon burst event (Fig. 4, smaller dots), taking into account the altitude-dependent, mean terminal velocities of the descending radiosonde system (Fig. 1a). For radiosonde 2017-3, communication was lost with the radiosonde during its ascent within the updraft before any significant negative accelerations occurred, and therefore, no adjustments were necessary.

Before the adjustments described above, the maximum $w_{\mathrm{air}}$ values measured by the radiosondes for the 2017 and 2016 cases were 36.2 and $25.5\,\mathrm{m\,s^{-1}}$, respectively. After adjusting for the balloon burst assumption for the 2017-1 and 2016-2 radiosondes, the respective maximum radiosonde $w_{\mathrm{air}}$ values were 45.8 and $49.9\,\mathrm{m\,s^{-1}}$. Here, it is important to emphasize that there is larger uncertainty in $w_{\mathrm{buoy}}$ after the balloon burst, in part due to the larger spread of descent rates that are used for the adjustments and that are based on the clear-air radiosondes after their balloons burst (Fig. 1a). However, making this adjustment provides a more realistic estimate of $w_{\mathrm{air}}$, assuming the radiosonde balloon does burst. Additional testing would be needed to quantify the uncertainties for these adjusted $w_{\mathrm{air}}$ estimates. In the next sections, we present the radiosonde $w_{\mathrm{air}}$ for each launch in the context of the radar data.

### *a. 2017 case*

Radiosonde 2017-1 was launched at 2158 UTC, shortly after the supercell formed and within the dual-Doppler analysis region for the CSU–CHILL and KFTG radars. Figure 6 depicts the radiosonde $w_{\mathrm{air}}$ along with two snapshots of the radiosonde position within the storm based on the radar reflectivity and dual-Doppler-derived $w_{\mathrm{air}}$. Based on the radiosonde humidity data, the radiosonde entered cloud around 2.7 km MSL, at which point $w_{\mathrm{air}}$, the updraft vertical velocity, was $5.5\,\mathrm{m\,s^{-1}}$. This corresponds to an average rate of acceleration from the ground level to cloud base of $0.034\,\mathrm{m\,s^{-2}}$. The radiosonde continued to accelerate within the cloudy updraft through ~7.5 km MSL at an average rate of $0.116\,\mathrm{m\,s^{-2}}$, more than triple the rate below cloud base, and the horizontal winds decreased from ~10 to $\sim 1\,\mathrm{m\,s^{-1}}$ and shifted from southerly to northerly (Figs. 4b,c).

During this time period, the radiosonde was located within the main updraft, along the western part of the weak echo region. At 7.5 km MSL (Figs. 6b–g), the radiosonde decelerated for ~15–20 s as it entered a region of higher reflectivity (>50 dbZ) and low correlation coefficients (<0.9, not shown), suggesting large hail (e.g., Balakrishnan and Zrnić 1990; Ryzhkov et al. 2013). Although the dual-Doppler analyses do not resolve the winds on the scales observed by the radiosonde, the fact that both dual-Doppler analyses (Figs. 6e,g) depict increasing $w_{\mathrm{air}}$ with height (which would suggest positive balloon acceleration as opposed to deceleration) supports our hypothesis that the balloon burst. As such, above 7.5 km MSL, adjustments were made to the $w_{\mathrm{air}}$ estimates using a $w_{\mathrm{buoy}}$ corresponding to a burst radiosonde balloon, as described in

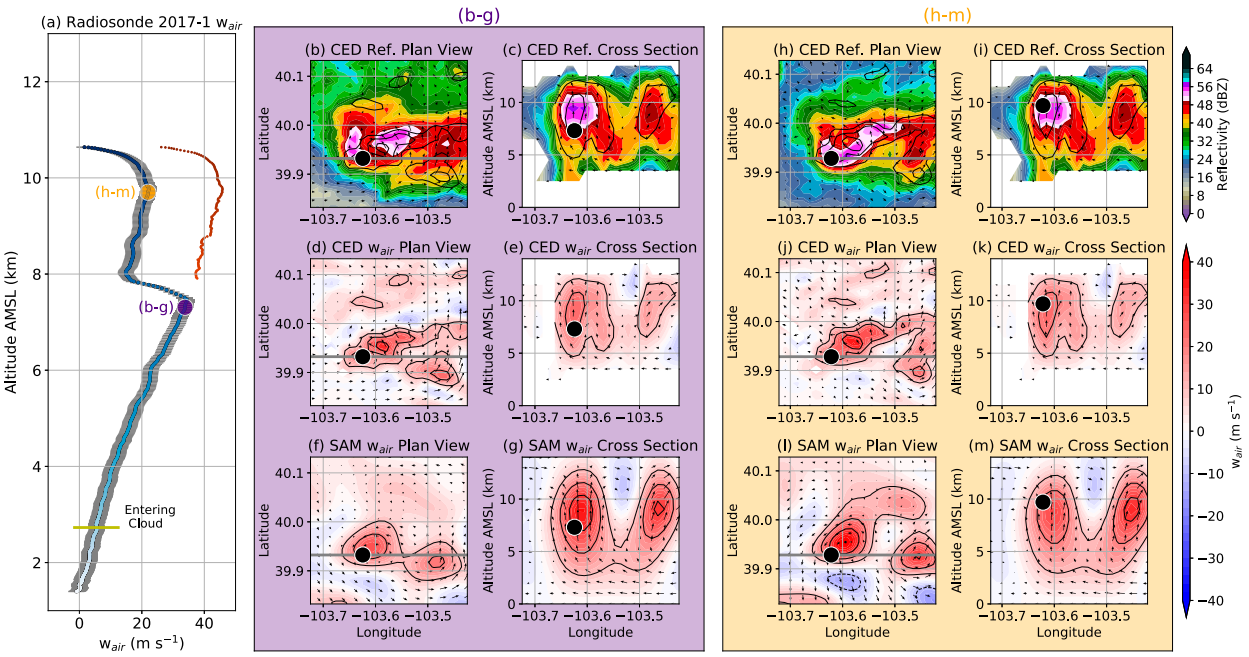


FIG. 6. (a) Radiosonde $w_{air}$ for the 2017-1 launch with uncertainty estimates (gray). The shading from light to dark blue represents the time evolution of the radiosonde from launch to maximum altitude. The smaller red dots take into account adjustments, assuming the radiosonde balloon burst. (b)–(m) The position of the radiosonde (black dots) within the storm at two different times during the radiosonde ascent. (top) Radar reflectivity plan views and vertical cross sections, as denoted by the gray lines in the plan views. Also shown are the plan views and cross sections of (middle) CEDRIC $w_{air}$ and (bottom) SAMURAI $w_{air}$. The arrows represent storm-relative winds in their respective planes, and black contours indicate 10 m s$^{-1}$ intervals of $w_{air}$, excluding the 0 m s$^{-1}$ contour.

the prior section. At 9.7 km MSL (Figs. 6h–m), the $w_{air}$ after adjustments reached its peak value (45.8 m s$^{-1}$). At this time, the radiosonde was within the primary updraft region but was nevertheless located ~5 km to the southwest of the most intense radar-derived updrafts (Figs. 6j,l), suggesting that the maximum $w_{air}$ in this storm was likely even higher than that estimated from the radiosonde. We note that the adjusted radiosonde $w_{air}$ values are more intense than those from the radar analyses, and the $w_{air}$ estimates from the different observing platforms are compared in section 5a. The radiosonde reached its maximum altitude of 10.6 km MSL after experiencing north-northwesterly winds for 2–3 min, which advected the radiosonde to the southern periphery of the updraft, where the $w_{air}$ was no longer strong enough to suspend the radiosonde system.

Approximately 1 h later (2251 UTC), another radiosonde (2017-2) was launched into the supercell updraft. Although the supercell was no longer within the region where dual-Doppler estimates could be made, both radar RHIs (not shown) and PPIs were used to contextualize the radiosonde measurements. Figure 7 shows PPI snapshots throughout the radiosonde trajectory at times when the radiosonde location was simultaneously sampled by one of the radars. The 2017-2 radiosonde was launched to the southwest of the WER (Fig. 7b), was advected northward in the inflow, and observed $w_{air}$ of ~14 m s$^{-1}$ before entering the cloud at 3.7 km MSL, which was above cloud base. A maximum $w_{air}$ of 36.2 m s$^{-1}$ was obtained at approximately 10.4 km MSL (Fig. 7e). Despite observing strong $w_{air}$ throughout its trajectory, the radiosonde was consistently located ~5–10 km to the southwest of where the strongest $w_{air}$ was likely located: the WER in the lower and middle troposphere (Figs. 7c,d) and the higher reflectivity regions in the upper troposphere (Fig. 7e). After reaching the top of the storm, the radiosonde underwent negative acceleration and sampled a minimum $w_{air}$ of −26.1 m s$^{-1}$, which was likely associated with strong downdrafts south of the main updraft (Fig. 7f). Unlike the 2017-1 radiosonde, 2017-2 eventually exited the storm (Fig. 7g) and rose to an altitude of 22.2 km MSL before the radiosonde balloon burst.

At 2359 UTC, a third radiosonde (2017-3; Fig. 8) was launched and subsequently sampled the WER in the middle troposphere (Figs. 8b,c). This radiosonde experienced the strongest vertical velocities between the surface and 6.8 km MSL of all three radiosondes from this case, accelerating at an average rate of 0.113 m s$^{-2}$ from 4.3 m s$^{-1}$ at 2 km MSL to a maximum $w_{air}$ of 31.1 m s$^{-1}$ at 7.1 km MSL. Unfortunately, the thermodynamic sensors were compromised during the radiosonde launch, and thus it is unclear at exactly which point the radiosonde entered cloudy conditions. Above 7.1 km MSL, the radiosonde began to decelerate and likely encountered rain and/or hail (Figs. 8a,d); communication with the radiosonde was lost at 10.8 km MSL.

### b. 2016 case

Similar analyses were conducted for radiosondes 2016-1 and 2016-2 for the isolated supercell that occurred on 17 July 2016. Because the supercell passed closer to the radar network

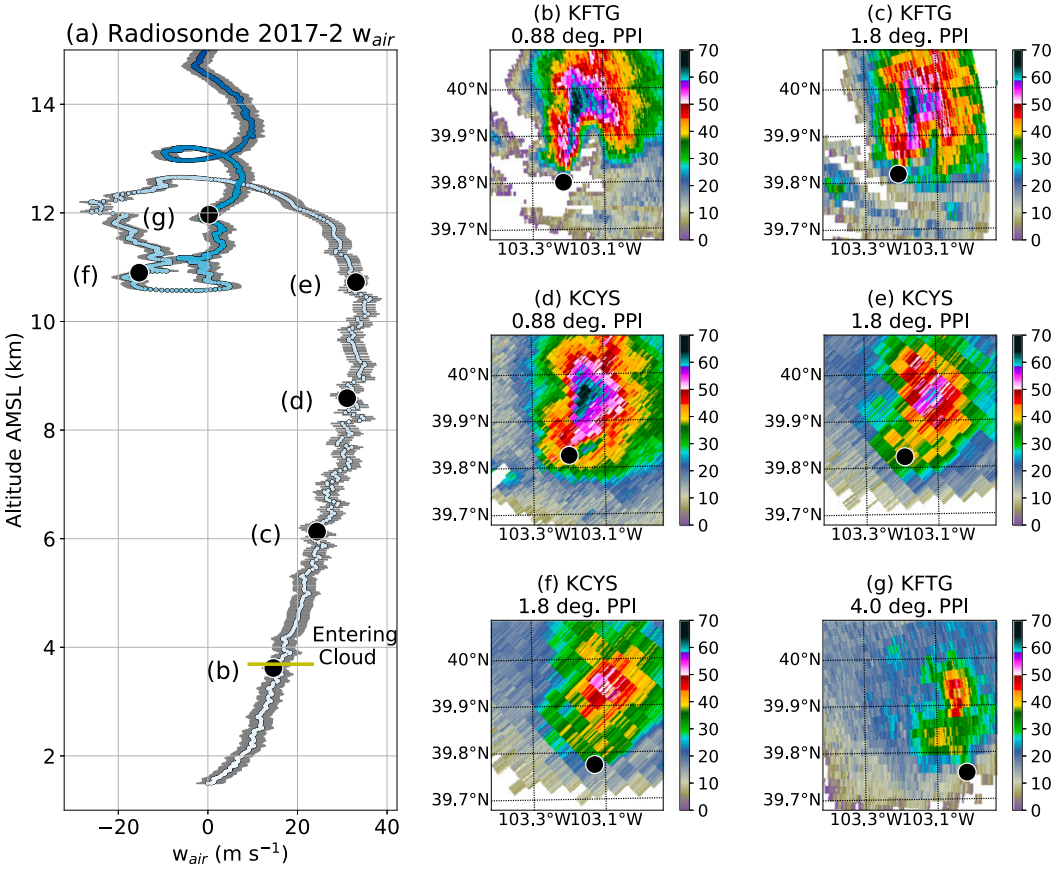


FIG. 7. (a) Radiosonde-derived $w_{air}$ for the 2017-2 launch with uncertainty estimates (gray). The shading from light to dark blue represents the time evolution of the radiosonde from launch to maximum altitude. (b)–(g) PPI scans of radar reflectivity that overlapped with the radiosonde within a 15 s window and within 500 m of the radiosonde's position, as labeled in (a).

(Fig. 3c), the dual-Doppler analyses were conducted with 500-m grid spacing, which allowed for a more detailed structure in the $w_{air}$ values, although the analyses were still unable to resolve the finer-scale motions observed by the radiosondes.

At 2224 UTC, the 2016-1 radiosonde (Figs. 9, 10) was launched on the southern side of the supercell, shortly after the cold pool associated with the rear flank downdraft passed the launch location, resulting in negative-to-neutral $w_{air}$ and northwesterly winds near the surface (Figs. 9a, 5). A radiosonde-based $w_{air}$ of $\sim 23\,m\,s^{-1}$ was observed twice during the radiosonde's ascent through the storm (at 6.8 and 9.1 km MSL; Fig. 9). In both instances, the radiosonde was in the extreme southwest edge of the updraft region, and ~10 km to the west of the WER (Figs. 9b,c,h,i). The radiosonde continued to rise above 12 km MSL and then underwent a 2.5-km descent, during which it observed a minimum $w_{air}$ of $-26.8\,m\,s^{-1}$ (Figs. 10b–g). This radiosonde, however, experienced its most intense negative acceleration immediately before the radiosonde's final descent to the surface (Fig. 5d), and therefore, we propose that this first radiosonde descent was associated with nearby, strong upper-level downdrafts that were diagnosed by both the SAMURAI analysis (Figs. 10f,g) and, to a lesser extent, the CEDRIC analysis (Figs. 10d,e) rather than with the balloon bursting. The radiosonde then experienced several vertical oscillations, ascending and descending three times around 10–11 km MSL and ~15 km to the southeast of the main updraft (Figs. 10h–m). These oscillations were likely associated with gravity waves in the anvil, which are evident in the CEDRIC analyses (Figs. 10j,k), but less so in the SAMURAI analyses (Figs. 10l,m) due to the filtering scales and different approaches used (section 2b). The relatively weak vertical motions in the anvil (Figs. 10j–m) would not have been strong enough to suspend the radiosonde had the balloon burst, providing further evidence that the balloon did not burst until right before the radiosonde's final descent to the surface.

At 2341 UTC, radiosonde 2016-2 was launched to the south of the WER (Fig. 11b) and was likely closer to the regions with the most intense vertical motions than was radiosonde 2016–1. This radiosonde experienced strong southerly winds, particularly between 6 and 8 km MSL, (Figs. 4b,c) that advected it toward the storm's updraft. At 8 km MSL, however, the radiosonde experienced its most intense negative acceleration

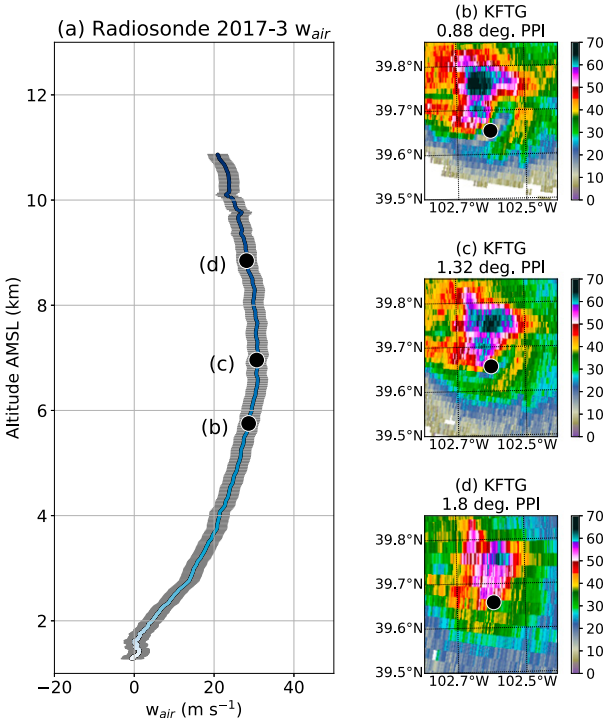


FIG. 8. As in Fig. 7, but for the 2017-3 radiosonde launch.

(Figs. 11a,c, 5e) and a significant decrease in horizontal wind speeds (Fig. 4b), while the radiosonde was entering a region to the north with high reflectivity (>50 dbZ) and correlation coefficients <0.94, which suggests large hail. Based on this evidence, we suspect that the balloon burst at this time right before being entrained into the storm's intense updraft. Therefore, adjustments were made to $w_{\text{air}}$ to account for this balloon burst assumption. However, we acknowledge that this 2016-2 balloon burst assumption is more uncertain than that for the 2017-1 balloon. The radiosonde measured a maximum estimated $w_{\text{air}}$ of 49.9 m s$^{-1}$ at 10.3 km MSL (Fig. 11a). Shortly after this maximum value was reached, the radiosonde was located within the region of maximum reflectivity at 12.1 km MSL (Fig. 11d). This suggests that the radiosonde was near some of the storm's most intense vertical motions, which were able to loft large hydrometeors to these near-tropopause heights. Considering the assumptions and adjustments for balloon bursting, 49.9 m s$^{-1}$ was the strongest vertical velocity observed by a radiosonde from these two C$^3$LOUD-Ex cases. This result is consistent with the fact that this radiosonde was launched in the most unstable (i.e., highest CAPE) environment of all the radiosondes (Fig. 3c; Table 1), as will be discussed in section 5b. It is important to restate that none of these estimates considers the impacts of hydrometeors, which would lead to both an underestimation of and an additional uncertainty in the $w_{\text{air}}$ values presented.

## 5. Comparisons of radiosonde $w_{\text{air}}$ to other platforms

### a. *Comparisons with dual-Doppler estimates*

In addition to contextualizing the radiosonde observations, the radar data also provide an independent estimate of $w_{\text{air}}$ for radiosondes 2017-1 and 2016-1. It is important to note the differences in the features that the two types of observing systems can resolve. The values in the dual-Doppler analyses represent the *average* vertical velocity over a cube with side

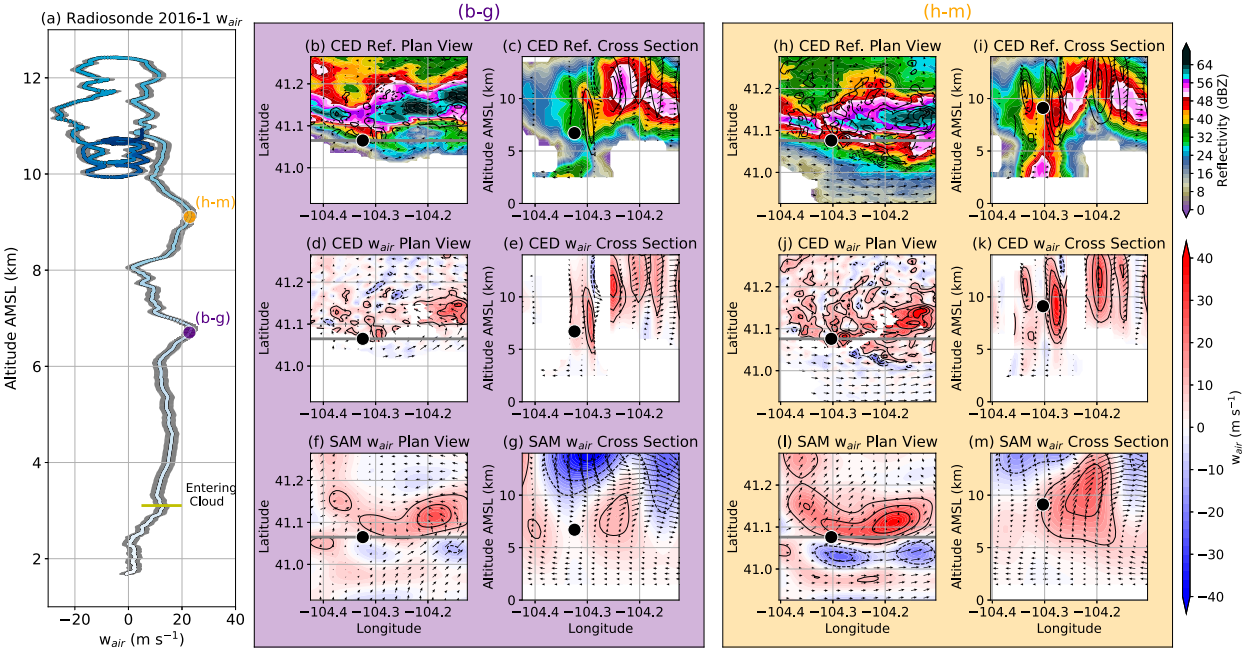


FIG. 9. As in Fig. 6, but for the radiosonde 2016-1 data. The light blue to dark blue shading in (a) represents the progression of time from launch to when the balloon likely burst.

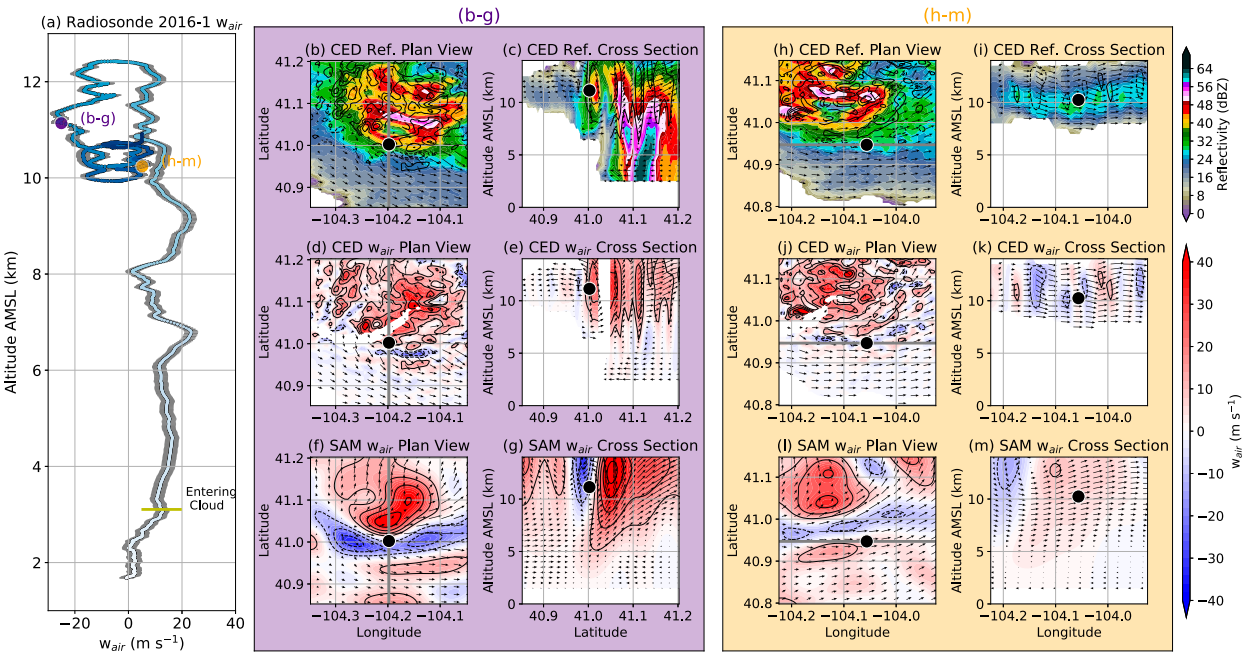


FIG. 10. As in Figs. 6 and 9, but for two later times during the progression of radiosonde 2016-1.

lengths of 1 km (500 m) for the 2017 (2016) case using data collected over a 5-min interval. The radiosonde values, however, represent averages along a slantwise path corresponding to the radiosonde trajectory over the course of the 12-s averaging period (e.g., horizontal and vertical distances generally between 150 and 700 m). Such differences need to be considered when comparing these estimates of vertical velocity obtained using these different platforms.

A comparison of radiosonde $w_{\text{air}}$ with the dual-Doppler $w_{\text{air}}$ from SAMURAI and CEDRIC is shown in Fig. 12. The dual-Doppler analyses for each radar volume were calculated at the volume-scan midpoint time and were advected in time using the calculated storm motion for each radar volume to create a 4D dataset. These 4D data were interpolated in time and space to the same position as the radiosonde for this comparison. To account for shifts in position within the dual-Doppler analyses that may be due to small advection errors, we also show the range of values in the surrounding grid boxes that are 1 km from the radiosonde location in the horizontal plane. This spread does not, however, represent any underlying uncertainty in the radar dual-Doppler analyses, which can come from a variety of sources as described in the introduction. In particular, the distance of these C$^3$LOUD-Ex storms from the radars, combined with the fixed NEXRAD radar scanning patterns, as well as the homogeneous advection corrections (e.g., Shapiro et al. 2010) could produce significant sources of error. However, these errors can only be quantified from additional observation system simulation experiments (OSSEs; e.g., Potvin et al. 2012; Oue et al. 2019; Dahl et al. 2019).

Comparisons cannot be made below 3.7 km MSL (Fig. 12a) and 6.0 km MSL (Fig. 12b) for the 2017 and 2016 cases, respectively, due to the lack of quality radar data at the radiosonde locations. This demonstrates one benefit of the radiosonde observations, namely their ability to sample vertical motions where radars only observe very low signal-to-noise ratios, such as below cloud base and along cloud

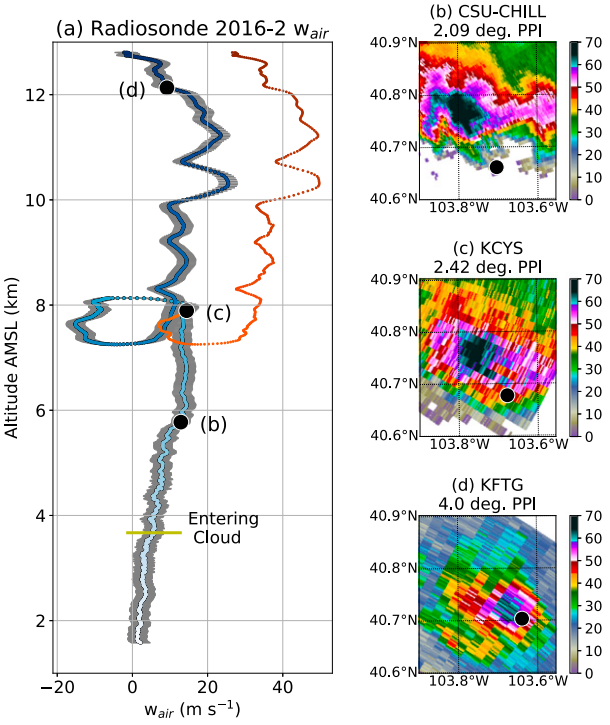


FIG. 11. As in Figs. 7 and 8, but for radiosonde 2016-2. The smaller red dots take into account adjustments assuming that the radiosonde balloon burst.

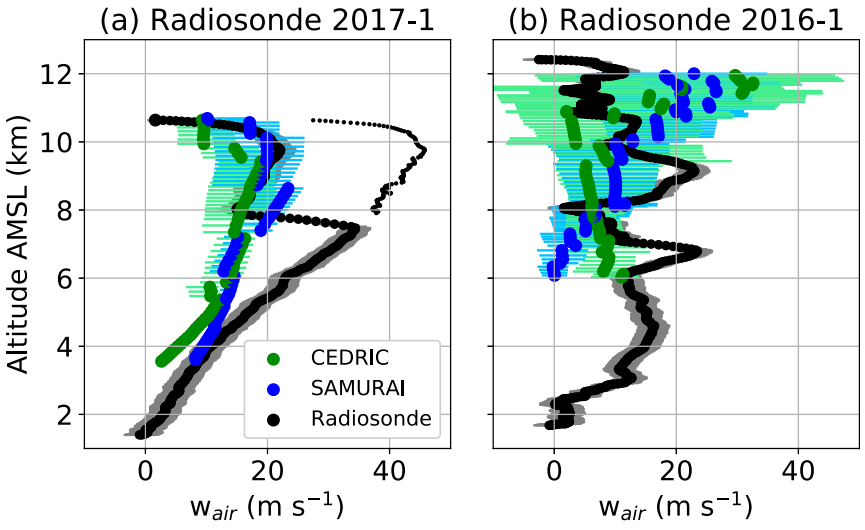


FIG. 12. Comparison of radiosonde and dual-Doppler $w_{air}$ for radiosondes (a) 2017-1 and (b) 2016-1, as described in the text. The gray range for the radiosonde data represents the quantified uncertainty in $w_{air}$. The green and blue dots represent the dual-Doppler analyses interpolated to the radiosonde position. The green and blue horizontal lines represent the range of values within 1 km in the horizontal direction of the radiosonde position within the dual-Doppler analyses.

edges. Based on the C$^3$LOUD-Ex radiosonde observations, $w_{air}$ can approach 20 m s$^{-1}$ in these regions.

Both dual-Doppler analyses show consistent trends and similar magnitudes of $w_{air}$. In both cases and for both dual-Doppler analyses, at the locations where the radiosondes observe the strongest $w_{air}$, the dual-Doppler $w_{air}$ values was generally 15–20 m s$^{-1}$ less than those derived from the radiosondes. For radiosonde 2017-1 (Fig. 12a), right before it is assumed that the balloon burst at 7.5 km MSL, the difference between the radiosonde $w_{air}$ and those of both dual-Doppler analyses was ~15–20 m s$^{-1}$. For radiosonde 2016-1 (Fig. 12b), similar differences were present at 6.8 and 9.1 km MSL. This dual-Doppler underestimation of $w_{air}$ as compared to the most intense radiosonde $w_{air}$ was at least partly due to the radiosonde capturing localized features that were unable to be resolved by the resolution of these radar analyses. However, without a detailed error estimation of the dual-Doppler syntheses obtained from OSSEs for these cases, we are unable to quantify how much of the differences are due to errors associated with the C$^3$LOUD-Ex radar network and scanning patterns (e.g., Oue et al. 2019) versus systematic differences in the observed quantities. Regardless, this comparison does demonstrate that a comprehensive analysis of $w_{air}$ would benefit from in situ measurements that can better capture highly localized conditions.

### b. *Comparisons with parcel theory*

Parcel theory can also be used to estimate the theoretical maximum possible vertical velocity due to its relationship with CAPE (e.g., Weisman and Klemp 1984):

$$w_{\mathrm{MLCAPE}} = \sqrt{2 \times \mathrm{MLCAPE}}. \qquad (4)$$

MLCAPE is chosen, as compared to other CAPE variants (e.g., surface-based or most-unstable), because it more realistically represents the air entering deep convective updrafts. The expression shown in Eq. (4) assumes that vertical accelerations are only forced by buoyancy and does not account for the negative impacts from condensate loading and entrainment. Equation (4) also does not consider the impacts of perturbation pressure gradients, which have been shown to decelerate updrafts within the upper levels of supercells where the maximum vertical velocities are achieved (Peters et al. 2019). Therefore, Eq. (4) likely overestimates the maximum vertical velocities in supercell updrafts.

To assess Eq. (4) with respect to the C$^3$LOUD-Ex observations, MLCAPE (0–90 hPa AGL) is calculated for each radiosonde launch. These calculations assume pseudoadiabatic ascent and account for the latent heating associated with freezing above the 0°C level by assuming that ice fraction linearly increases from 0° to −40°C. While the subcloud-layer radiosonde data sampled by the updraft radiosondes are generally representative of the environmental air entering the supercell updraft, the data within the cloudy updraft are no longer representative of the environmental conditions needed to estimate MLCAPE. Therefore, the thermodynamic data from lowest levels of the updraft soundings were merged with data from the middle and upper levels of the environmental soundings (Figs. 3b,d). This concatenation occurred at the altitude where the temperature profiles first overlapped for each pair of soundings, near the inversion of the environmental sounding between 700 and 800 hPa. In cases where the radiosonde was launched in a cold pool or the thermodynamic data were not available (radiosondes 2016–1, 2017–1, and 2017–3), the closest, representative radiosonde launch in time and space was used as a better estimate of the inflow air for that

TABLE 1. The 0–90 hPa AGL MLCAPE, the theoretical maximum $w_{MLCAPE}$ based on Eq. (4), and comparisons with the maximum radiosonde $w_{air}$ for each radiosonde launch. For instances where the assumption of a balloon burst was used, two values are shown. The first represents the value including the balloon burst assumption, while the second, in parentheses, represents the value without adjusting for a balloon burst.

| Radiosonde | MLCAPE ($J\,kg^{-1}$) | $w_{MLCAPE}$ ($m\,s^{-1}$) | Maximum radiosonde $w_{air}$ ($m\,s^{-1}$) | Ratio of $w_{air}$ to $w_{MLCAPE}$ (%) |
|---|---|---|---|---|
| 2017-1 | 1313 | 51.2 | 45.8 (34.4) | 89.4 (67.2) |
| 2017-2 | 1172 | 48.4 | 36.2 | 74.9 |
| 2017-3 | 952 | 43.6 | 31.1 | 71.4 |
| 2016-1 | 1510 | 55.6 | 23.4 | 42.2 |
| 2016-2 | 2305 | 67.9 | 49.9 (25.5) | 73.5 (37.6) |

radiosonde launch, since we are interested in estimating the theoretical maximum vertical velocities.

Overall, the $w_{MLCAPE}$ values calculated via parcel theory were larger than the $w_{air}$ values observed by the radiosondes (Table 1). Further, these results highlight the variability of $w_{air}$ within the primary supercell updraft. The ratio of $w_{air}$ to $w_{MLCAPE}$ ranges from 42% to 89%, largely due to the variability in the positions sampled within the supercell updrafts. When the balloon burst assumption is not considered, the ratios for radiosondes 2017-1 and 2016-2 fall from 89% to 67% and from 74% to 38%, respectively. Assuming the correct identification and adjustments for balloon bursts, the radiosonde with the smallest ratio (42%, 2016-1) sampled the extreme western edge of the primary updraft, ~10 km from the WER (Fig. 9). The radiosonde with the largest ratio (89%, 2017-1) sampled close to where the most intense vertical motions were likely located (Fig. 6). While the maximum vertical velocities estimated from these radiosonde data do not reach their theoretical maxima, as predicted by Eq. (4), a larger sample of observations, especially those similar to radiosonde 2017-1 that sampled near the most intense $w_{air}$, is needed to better observationally assess the relationship shown in Eq. (4).

## 6. Implications for future in situ observations of $w_{air}$ within storms

This study has shown that GPS sensors aboard radiosondes can provide useful in situ observations of $w_{air}$ within storms, especially when used in conjunction with radar data. Understanding the position within the updraft being sampled by the radiosonde provided valuable context for interpreting the radiosonde observations. Particularly with GPS radiosondes that can directly transmit their locations while sampling, coordinated scanning of radars through the use of PPIs and RHIs to the exact positions of airborne radiosondes should be considered for future field campaigns. For example, using these collocated radar and radiosonde observations, we demonstrated that most of the radiosonde measurements were likely several kilometers away from the strongest $w_{air}$ in these two supercell updrafts. Obtaining large samples of in situ observations in the locations of strongest $w_{air}$ within storms continues to be challenge, but forgoing cost constraints, this sampling difficulty can be alleviated by launching a high number of GPS sensors into storms (e.g., Markowski et al. 2018) so as to increase the probability of sampling the most intense vertical motions. This would also simultaneously improve the spatial coverage of these in situ measurements.

While several of the uncertainties in the radiosonde-based $w_{air}$ were quantified in this study, we did not quantify the uncertainty associated with hydrometeor collisions and collection on the radiosonde system. Innovative techniques and technologies to minimize or quantify these hydrometeor impacts would improve radiosonde observations within cloud systems. For example, cameras have been placed on radiosondes to assess icing impacts on in situ observations within winter storms (Waugh and Schuur 2018), and similar strategies could potentially be used to observe the possible accumulation of hydrometeors on the radiosonde system within updrafts. Furthermore, we analyzed balloon accelerations and assumed, with contextual support, that the radiosonde balloon burst when it experienced its most negative accelerations, in order to obtain a better estimate of $w_{air}$. However, this assumption was more uncertain for radiosonde 2016-2 due to the less clear trajectory and more turbulent conditions, as compared with radiosonde 2017-1. Additional sensors could be introduced to the radiosonde system to assist in assessing balloon burst events, which would reduce these uncertainties.

## 7. Conclusions

One of the goals of the $C^3$LOUD-Ex field campaign was to obtain in situ observations of the vertical velocities of supercell updrafts ($w_{air}$) with targeted radiosonde launches. In situ observations of supercell vertical velocities have been limited, despite their importance for understanding physical processes within supercells and for verifying simulations as well as other observational platforms with difficult-to-characterize uncertainties. In this study, we present observations of $w_{air}$ from two isolated supercell cases observed during $C^3$LOUD-Ex, which occurred in the High Plains of Colorado, Wyoming, and Nebraska. Radiosonde $w_{air}$ estimates were based on GPS data and were calculated with an uncertainty of $\pm 2.6\,m\,s^{-1}$, which considered uncertainties associated with the GPS measurements themselves, the helium balloon buoyancy, and varying drag forces. These estimates, however, did not consider hydrometeor impacts on the radiosonde systems which could be significant and would lead to an underestimation of the $w_{air}$ presented in this study.

In two of the five updraft radiosonde launches assessed in this study, we inferred that the radiosonde balloon burst while within the updraft, based on the extrema in the radiosonde negative accelerations. In these instances, we adjusted the $w_{air}$ estimates to account for the loss of buoyancy associated with

balloon bursting. Before these adjustments, the maximum radiosonde $w_{air}$ was 36.2 m s$^{-1}$ at an altitude of 10.4 km MSL during the 2017 case. After these adjustments, the maximum $w_{air}$ that was observed was 49.9 m s$^{-1}$ at an altitude of 10.3 km MSL during the 2016 case, which occurred in the most unstable environment. At the lower and middle tropospheric levels, radiosonde 2017-3 captured the greatest $w_{air}$ and was located within the WER, reaching a maximum value of 31.1 m s$^{-1}$ at 7.1 km MSL. In most of the observations presented, the radar data suggested that the radiosondes were several km away from the strongest $w_{air}$ within the supercell updraft. This fact, along with the potential impacts of hydrometeors on the radiosonde systems, suggests that the maximum $w_{air}$ in these two supercells was likely even larger than the values reported here.

The C$^3$LOUD-Ex radiosonde observations were also compared with other methods of obtaining $w_{air}$. One radiosonde in each of the two supercell cases sampled the updraft within the regions where dual-Doppler analyses could be performed, allowing for an independent measure of $w_{air}$. For the locations where the radiosondes observed the greatest $w_{air}$, the dual-Doppler $w_{air}$ values were generally 15–20 m s$^{-1}$ less than the radiosonde estimated $w_{air}$ values. This was at least partly due to the different scales being observed by these two platforms, although it was difficult to fully quantify these differences without a detailed assessment of the dual-Doppler errors, such as may be obtained through the use of OSSEs, and which is left for future work. However, these comparisons did demonstrate that radiosondes provide complementary data to multi-Doppler analyses in terms of their ability to sample regions with low signal-to-noise ratios and to provide localized, high-resolution observations, both of which can be challenging in multi-Doppler analyses. When the balloon burst correction was included, the maximum radiosonde-based $w_{air}$ values were 42%–89% of the theoretical maximum $w_{air}$ from parcel theory. The variability in these comparisons was primarily due to the locations within the broad supercell updrafts that were sampled by the radiosondes, which were ascertained using collocated radar data.

Some of the challenges associated with making radiosonde observations of updrafts were highlighted here, and additional ideas on how these challenges can be surmounted were provided. There continues to be large uncertainty in the vertical velocities within deep convection, which are important for understanding many atmospheric processes and improving models. In situ observations of $w_{air}$ can complement remotely sensed estimates both by providing both an independent measure of $w_{air}$ for comparison and by observing finer-scale motions that often cannot be resolved using remote sensing. As such, despite their relative scarcity, in situ observations of $w_{air}$ can contribute to a more comprehensive understanding of storm vertical motions and hence should be considered for future field campaigns.

*Acknowledgments.* Funding from the Monfort Excellence Fund provided to Susan C. van den Heever as a Monfort Professor at Colorado State University is acknowledged, as well as funding from NSF grants AGS-1409686 and AGS-2019947. Peter Marinescu, Sean Freeman, and Aryeh Drager were also partially supported by NSF Grant No. DGE-1321845 Amend 5 and NSF Grant No. DGE-1840343. Michael Bell was supported by NSF Grants AGS-1701225 and OAC-1661663. We would like to acknowledge the entire C$^3$LOUD-Ex science team for their time and efforts, particularly Dr. Emily Riley Dellaripa for assisting in the initial discussions for this work. We would also like to acknowledge Mark Benoit from InterMet systems for assisting with the radiosonde system and Dr. Stacey Hitchcock for useful discussions. We thank Dr. Nathan Dahl and two anonymous reviewers for their constructive and thorough feedback on this work.

*Data availability statement.* The radar and radiosonde data analyzed in this manuscript are all available upon request. The HRRR data were obtained from an archive of the High Resolution Rapid Refresh model (doi:10.7278/S5JQ0Z5B).

## APPENDIX A

### Power Spectra Analysis of Radiosonde Velocity Data

To determine the choice of $\Delta t$, power spectra were computed for all the clear air and updraft radiosonde launches presented in this manuscript. The vertical wind speeds ($w_{air}$), horizontal wind speed ($h_{spd}$), and horizontal wind direction ($h_{dir}$) were first calculated with a $\Delta t$ of 2 s, using the GPS data from the position 1 s before and after the current position. Power spectra analyses, following the methodology in Marinescu et al. (2019), were then conducted on these data. To summarize this methodology, these 1-Hz data were broken down into data chunks that were 180 s long and accurately resolved periodic signals from 2 to 90 s. These data chunking resulted in anywhere from 5 to 49 data chunks for each radiosonde launch, and the power spectra from these data chunks were then averaged together to create a better statistical representation of the periodic signals within each launch's data (thin lines in Fig. A1). The power spectra from each radiosonde launch were also combined for all the clear air, updraft, and all launches, respectively, and averaged (thick lines in Fig. A1). Red-noise power spectra were estimated using the average lag-1 autocorrelations from these data groups, as a reference for these data without any periodic signals (Gilman et al. 1963). A periodic signal in the observed data is interpreted to be present if the data has more power than the red-noise power spectra for that period. From these analyses, it is clear that periodic signals are present in this data on time scales of ~12 s and less in all the wind data. These results are consistent with the theoretical calculation of the ~11–12-s period of a pendulum with a 30-m string, which represents the length of the radiosonde dereeler using during C$^3$LOUD-Ex. Interestingly, the updraft launches (red, thick line) have more consistent periodic signals with periods between 6.0 and 6.5 s in the wind speeds, while the clear-air launches have more consistent signals between 9–12, 5, and 3.3 s, suggesting slight differences in the radiosondes' periodic motions between these two conditions. Overall, these power spectra guided the choice of using a $\Delta t$ of 12 s, which substantially reduced the contribution of these periodic signals with

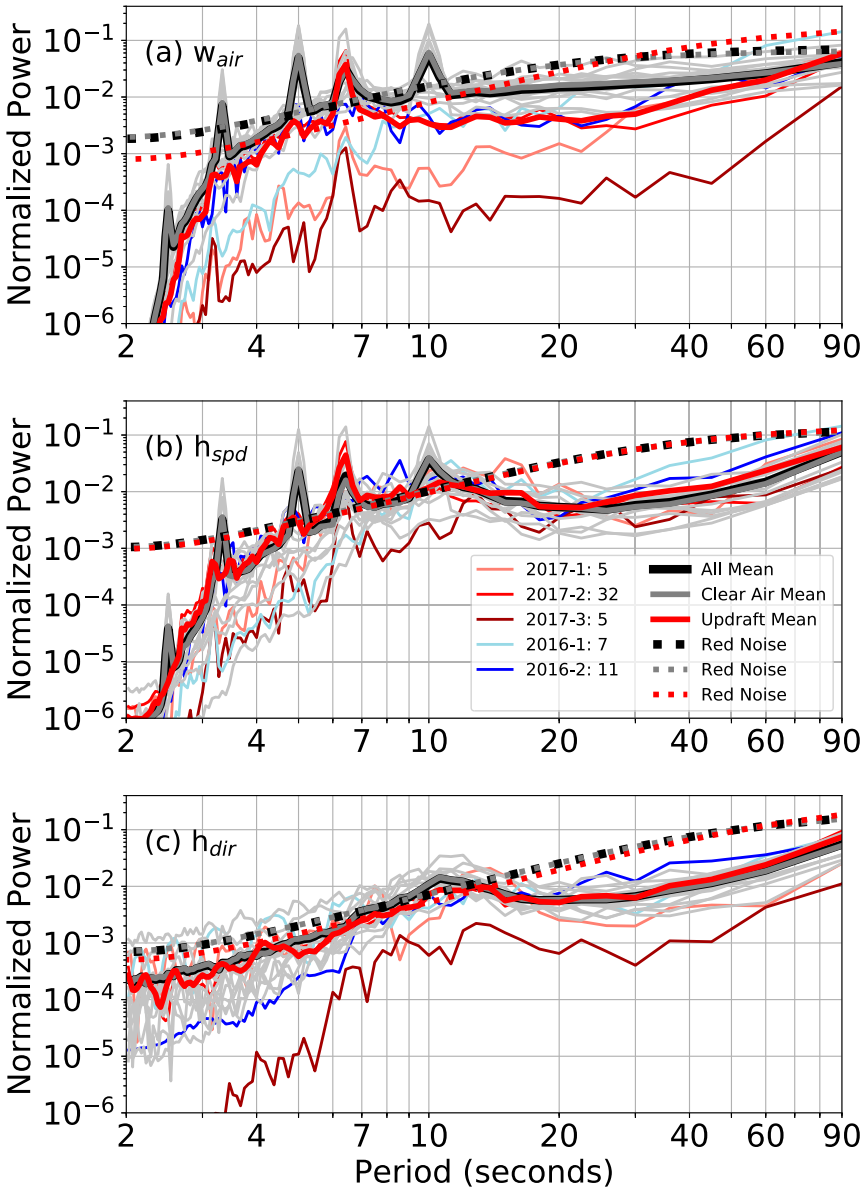


FIG. A1. Mean power spectra for the 13 clear-air (thin gray lines) and 5 updraft (thin red and blue lines) radiosonde launches for (a) $w_{air}$, (b) $h_{spd}$, and (c) $h_{dir}$. The data chunk that was used was 180 s, and the number of chunks that went into each radiosonde launch is shown in the legend. For the 13 clear-air launches, the number of chunks varied from 18 to 49. The thick solid black line represents the mean power spectra for all the data, while the thick solid gray and red lines represent the means of the clear-air and updraft launches, respectively. Estimates of the red noise spectra are also shown as thick dashed lines.

time scales of 12 s and less in the updraft $w_{air}$ calculations, while still allowing for finer-scale observations and error propagation analyses.

## APPENDIX B

### Analysis of $\epsilon_{w,\text{upd-drag}}$

The term $\epsilon_{w,\text{upd-drag}}$ is the uncertainty in the $w_{air}$ estimate arising from changes in the drag force on the radiosonde system within an updraft as compared to still-air conditions. Because radiosonde systems typically reach their terminal velocity within a couple of seconds and are often close to terminal-velocity balance, we can use the formula for the terminal velocity and its dependence on the drag coefficient ($C_D$) to estimate the uncertainty.

The terminal velocity ($v_T$) of the radiosonde system can be determined as follows (following, e.g., Wang et al. 2009; Gallice et al. 2011):

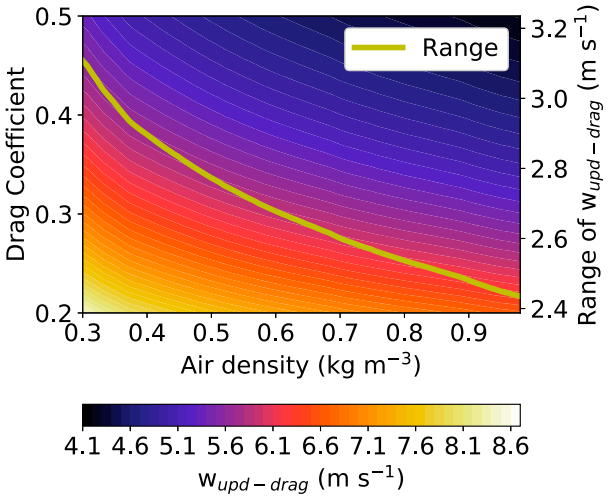


FIG. B1. Terminal velocity calculations (m s$^{-1}$) for ascending C$^3$LOUD-Ex radiosondes with varying drag coefficients and densities (shaded, left axis) and the range (maximum minus minimum) of terminal velocities for each density (right axis).

$$v_T = \sqrt{\frac{2g(\text{net free lift})}{\rho C_D A}} \tag{B1}$$

In Eq. (B1), net free lift (units of kg), when multiplied by acceleration due to gravity $g \sim 9.81\,\text{m s}^{-2}$, is the upward buoyant force acting on the radiosonde system. Net free lift is calculated as the difference of two quantities: 1) the mass measured when the helium-filled balloon is attached to a spring scale (typical value of 1.03 kg; range from 0.86 to 1.40 kg); and 2) the combined mass of the radiosonde and dereeler attached to the balloon (0.24 kg). These measurements were taken during the clear-sky, still-air launches described in section 2a. The other variables in Eq. (B1) include the ambient air density $\rho$, the drag coefficient $C_D$, and balloon cross-sectional area $A$. The helium inside the balloon is assumed to expand adiabatically as the balloon rises. The initial $A$ of the balloon is approximately 1.33 m$^2$, obtained from the clear-sky, still-air launches. Based on prior laboratory studies using perfect spheres (Achenbach 1972; Son et al. 2010) and on radiosonde observations during relatively calm, nighttime conditions (Gallice et al. 2011), drag coefficients for tropospheric conditions generally fall between 0.2 and 0.5. The drag coefficient within a supercell updraft may fall outside of this range, but we have no way of knowing whether this is the case due to the lack of observations. Using the known range of tropospheric drag coefficients from relatively calm conditions and using a range of tropospheric air densities, we can estimate the uncertainty of $v_T$, and thus $w_{\text{air}}$, due to variations in $C_D$ based on Eq. (B1) (Fig. B1). The range of $v_T$ as a function of air density (gold line) is at most 3.1 m s$^{-1}$, which occurs at the lowest density included (0.3 kg m$^{-3}$, representative of the upper troposphere). Therefore, we estimate that $\epsilon_{w,\text{upd-drag}}$ is $\pm 1.6\,\text{m s}^{-1}$, which is half of the maximum range (3.1 m s$^{-1}$).

## REFERENCES


Achenbach, E., 1972: Experiments on the flow past spheres at very high Reynolds numbers. *J. Fluid Mech.*, **54**, 565–575, https://doi.org/10.1017/S0022112072000874.

Armijo, L., 1969: A theory for the determination of wind and precipitation velocities with Doppler radars. *J. Atmos. Sci.*, **26**, 570–573, https://doi.org/10.1175/1520-0469(1969)026<0570:ATFTDO>2.0.CO;2.

Balakrishnan, N., and D. S. Zrnić, 1990: Use of polarization to characterize precipitation and discriminate large hail. *J. Atmos. Sci.*, **47**, 1525–1540, https://doi.org/10.1175/1520-0469(1990)047<1525:UOPTCP>2.0.CO;2.

Barnes, S. L., 1970: Some aspects of a severe, right-moving thunderstorm deduced from mesonetwork rawinsonde observations. *J. Atmos. Sci.*, **27**, 634–648, https://doi.org/10.1175/1520-0469(1970)027<0634:SAOASR>2.0.CO;2.

Bell, M. M., M. T. Montgomery, and K. A. Emanuel, 2012: Air–sea enthalpy and momentum exchange at major hurricane wind speeds observed during CBLAST. *J. Atmos. Sci.*, **69**, 3197–3222, https://doi.org/10.1175/JAS-D-11-0276.1.

Bluestein, H. B., E. W. McCaul, G. P. Byrd, and G. R. Woodall, 1988: Mobile sounding observations of a tornadic storm near the dryline: The Canadian, Texas, storm of 7 May 1986. *Mon. Wea. Rev.*, **116**, 1790–1804, https://doi.org/10.1175/1520-0493(1988)116<1790:MSOOAT>2.0.CO;2.

——, ——, ——, ——, G. Martin, S. Keighton, and L. C. Showell, 1989: Mobile sounding observations of a thunderstorm near the dryline: The Gruver, Texas, storm complex of 25 May 1987. *Mon. Wea. Rev.*, **117**, 244–250, https://doi.org/10.1175/1520-0493(1989)117<0244:MSOOAT>2.0.CO;2.

Bousquet, O., P. Tabary, and J. Parent du Châtelet, 2008: Operational multiple-Doppler wind retrieval inferred from long-range radial velocity measurements. *J. Appl. Meteor. Climatol.*, **47**, 2929–2945, https://doi.org/10.1175/2008JAMC1878.1.

Browning, K. A., and F. H. Ludlam, 1962: Airflow in convective storms. *Quart. J. Roy. Meteor. Soc.*, **88**, 117–135, https://doi.org/10.1002/qj.49708837602.

——, and G. B. Foote, 1976: Airflow and hail growth in supercell storms and some implications for hail suppression. *Quart. J. Roy. Meteor. Soc.*, **102**, 499–533, https://doi.org/10.1002/qj.49710243303.

Brunkow, D., V. N. Bringi, P. C. Kennedy, S. A. Rutledge, V. Chandrasekar, E. A. Mueller, and R. K. Bowie, 2000: A description of the CSU–CHILL national radar facility. *J. Atmos. Oceanic Technol.*, **17**, 1596–1608, https://doi.org/10.1175/1520-0426(2000)017<1596:ADOTCC>2.0.CO;2.

Bryan, G. H., 2008: getcape. Accessed 1 July 2019, https://www2.mmm.ucar.edu/people/bryan/Code/getcape.F.

Chisholm, A. J., 1970: Alberta hailstorms: A radar study and model. Ph.D. thesis, McGill University, 237 pp.

——, 1973: Alberta hailstorms Part I: Radar case studies and airflow models. *Alberta Hailstorms*, *Meteor. Monogr.*, No. 36, Amer. Meteor. Soc., 1–36.

Collis, S., A. Protat, and K.-S. Chung, 2010: The effect of radial velocity gridding artifacts on variationally retrieved vertical velocities. *J. Atmos. Oceanic Technol.*, **27**, 1239–1246, https://doi.org/10.1175/2010JTECHA1402.1.

Dahl, N. A., A. Shapiro, C. K. Potvin, A. Theisen, J. G. Gebauer, A. D. Schenkman, and M. Xue, 2019: High-resolution, rapid-scan dual-Doppler retrievals of vertical velocity in a simulated supercell. *J. Atmos. Oceanic Technol.*, **36**, 1477–1500, https://doi.org/10.1175/JTECH-D-18-0211.1.

Davies-Jones, R. P., 1974: Discussion of measurements inside high-speed thunderstorm updrafts. *J. Appl. Meteor.*, **13**, 710–717,

https://doi.org/10.1175/1520-0450(1974)013<0710:DOMIHS>2.0.CO;2.

——, and J. H. Henderson, 1975: Updraft properties deduced statistically from Rawin soundings. *Pure Appl. Geophys.*, **113**, 787–801, https://doi.org/10.1007/BF01592959.

DiGangi, E. A., D. R. MacGorman, C. L. Ziegler, D. Betten, M. Biggerstaff, M. Bowlan, and C. K. Potvin, 2016: An overview of the 29 May 2012 Kingfisher supercell during DC3. *J. Geophys. Res. Atmos.*, **121**, 14 316–14 343, https://doi.org/10.1002/2016JD025690.

Dolan, B., and S. A. Rutledge, 2010: Using CASA IP1 to diagnose kinematic and microphysical interactions in a convective storm. *Mon. Wea. Rev.*, **138**, 1613–1634, https://doi.org/10.1175/2009MWR3016.1.

Fan, J., and Coauthors, 2017: Cloud-resolving model intercomparison of an MC3E squall line case: Part I—Convective updrafts. *J. Geophys. Res. Atmos.*, **122**, 9351–9378, https://doi.org/10.1002/2017JD026622.

Farley, R. E., 2005: BalloonAscent: 3-D simulation tool for the ascent and float of high-altitude balloons. *AIAA Fifth Aviation, Technology, Integration, and Operations Conf.*, Reston, VA, AIAA, 15 pp.

Foote, G. B., and J. C. Fankhauser, 1973: Airflow and moisture budget beneath a northeast Colorado hailstorm. *J. Appl. Meteor.*, **12**, 1330–1353, https://doi.org/10.1175/1520-0450(1973)012<1330:AAMBBA>2.0.CO;2.

Gal-Chen, T., 1978: A method for the initialization of the anelastic equations: Implications for matching models with observations. *Mon. Wea. Rev.*, **106**, 587–606, https://doi.org/10.1175/1520-0493(1978)106<0587:AMFTIO>2.0.CO;2.

Gallice, A., F. G. Wienhold, C. R. Hoyle, F. Immler, and T. Peter, 2011: Modeling the ascent of sounding balloons: Derivation of the vertical air motion. *Atmos. Meas. Tech.*, **4**, 2235–2253, https://doi.org/10.5194/amt-4-2235-2011.

Gao, J., M. Xue, A. Shapiro, and K. K. Droegemeier, 1999: A variational method for the analysis of three-dimensional wind fields from two Doppler radars. *Mon. Wea. Rev.*, **127**, 2128–2142, https://doi.org/10.1175/1520-0493(1999)127<2128:AVMFTA>2.0.CO;2.

Geerts, B., and Coauthors, 2018: Recommendations for in situ and remote sensing capabilities in atmospheric convection and turbulence. *Bull. Amer. Meteor. Soc.*, **99**, 2463–2470, https://doi.org/10.1175/BAMS-D-17-0310.1.

Gilman, D. L., F. J. Fuglister, and J. M. Mitchell, 1963: On the power spectrum of "red noise." *J. Atmos. Sci.*, **20**, 182–184, https://doi.org/10.1175/1520-0469(1963)020<0182:OTPSON>2.0.CO;2.

Helmus, J. J., and S. M. Collis, 2016: The Python ARM Radar Toolkit (Py-ART), a library for working with weather radar data in the Python programming language. *J. Open Res. Software*, **4**, e25, https://doi.org/10.5334/jors.119.

Heymsfield, A. J., and D. J. Musil, 1982: Case study of a hailstorm in Colorado. Part II: Particle growth processes at mid-levels deduced from in-situ measurements. *J. Atmos. Sci.*, **39**, 2847–2866, https://doi.org/10.1175/1520-0469(1982)039<2847:CSOAHI>2.0.CO;2.

InterMet Systems, 2016: iMet-1-ABxn data sheet. Grand Rapids Michigan, 1 pp., https://www.intermetsystems.com/ee/pdf/202060_iMet-1-ABxn_Data_161006.pdf.

Kropfli, R. A., and L. J. Miller, 1976: Kinematic structure and flux quantities in a convective storm from dual-Doppler radar observations. *J. Atmos. Sci.*, **33**, 520–529, https://doi.org/10.1175/1520-0469(1976)033<0520:KSAFQI>2.0.CO;2.

Lehmiller, G. S., H. B. Bluestein, P. J. Neiman, F. M. Ralph, and W. F. Feltz, 2001: Wind structure in a supercell thunderstorm as measured by a UHF wind profiler. *Mon. Wea. Rev.*, **129**, 1968–1986, https://doi.org/10.1175/1520-0493(2001)129<1968:WSIAST>2.0.CO;2.

Marinescu, P. J., S. C. van den Heever, S. M. Saleeby, and S. M. Kreidenweis, 2016: The microphysical contributions to and evolution of latent heating profiles in two MC3E MCSs. *J. Geophys. Res. Atmos.*, **121**, 7913–7935, https://doi.org/10.1002/2016JD024762.

——, E. J. T. Levin, D. Collins, S. M. Kreidenweis, and S. C. van den Heever, 2019: Quantifying aerosol size distributions and their temporal variability in the Southern Great Plains, USA. *Atmos. Chem. Phys.*, **19**, 11 985–12 006, https://doi.org/10.5194/acp-19-11985-2019.

Markowski, P. M., Y. P. Richardson, S. J. Richardson, and A. Petersson, 2018: Aboveground thermodynamic observations in convective storms from balloonborne probes acting as pseudo-Lagrangian drifters. *Bull. Amer. Meteor. Soc.*, **99**, 711–724, https://doi.org/10.1175/BAMS-D-17-0204.1.

Marshall, T. C., W. D. Rust, and M. Stolzenburg, 1995: Electrical structure and updraft speeds in thunderstorms over the southern Great Plains. *J. Geophys. Res.*, **100**, 1001–1015, https://doi.org/10.1029/94JD02607.

Marwitz, J. D., 1972: The structure and motion of severe hailstorms. Part I: Supercell storms. *J. Appl. Meteor.*, **11**, 166–179, https://doi.org/10.1175/1520-0450(1972)011<0166:TSAMOS>2.0.CO;2.

——, 1973: Trajectories within the weak echo regions of hailstorms. *J. Appl. Meteor.*, **12**, 1174–1182, https://doi.org/10.1175/1520-0450(1973)012<1174:TWTWER>2.0.CO;2.

——, and E. X. Berry, 1971: The airflow within the weak echo region of an Alberta hailstorm. *J. Appl. Meteor.*, **10**, 487–492, https://doi.org/10.1175/1520-0450(1971)010<0487:TAWTWE>2.0.CO;2.

Miller, L. J., 1975: Internal airflow of a convective storm from dual-Doppler radar measurements. *Pure Appl. Geophys.*, **113**, 765–785, https://doi.org/10.1007/BF01592958.

——, and S. M. Fredrick, 1998: CEDRIC custom editing and display of reduced information in Cartesian space. NCAR, 130 pp., https://www.eol.ucar.edu/system/files/cedric_doc.pdf.

Mullendore, G. L., D. R. Durran, and J. R. Holton, 2005: Cross-tropopause tracer transport in midlatitude convection. *J. Geophys. Res.*, **110**, D06113, https://doi.org/10.1029/2004JD005059.

Musil, D. J., A. J. Heymsfield, and P. L. Smith, 1986: Microphysical characteristics of a well-developed weak echo region in a high plains supercell thunderstorm. *J. Climate Appl. Meteor.*, **25**, 1037–1051, https://doi.org/10.1175/1520-0450(1986)025<1037:MCOAWD>2.0.CO;2.

National Centers for Environmental Information (NCEI), 2016: NCDC storm events database (storm data). NOAA, accessed 13 February 2020, https://www.ncdc.noaa.gov/stormevents/.

——, 2017: NCDC storm events database (storm data). NOAA, accessed 13 February 2020, https://www.ncdc.noaa.gov/stormevents/.

Nelson, S. P., and R. A. Brown, 1987: Error sources and accuracy of vertical velocities computed from multiple-Doppler radar measurements in deep convective storms. *J. Atmos. Oceanic Technol.*, **4**, 233–238, https://doi.org/10.1175/1520-0426(1987)004<0233:ESAAOV>2.0.CO;2.

Ooyama, K. V., 2002: The cubic-spline transform method: Basic definitions and tests in a 1D single domain. *Mon.*

*Wea. Rev.*, **130**, 2392–2415, https://doi.org/10.1175/1520-0493(2002)130<2392:TCSTMB>2.0.CO;2.

Oue, M., P. Kollias, A. Shapiro, A. Tatarevic, and T. Matsui, 2019: Investigation of observational error sources in multi-Doppler-radar three-dimensional variational vertical air motion retrievals. *Atmos. Meas. Tech.*, **12**, 1999–2018, https://doi.org/10.5194/amt-12-1999-2019.

Palmer, A. D. F., 1912: *The Theory of Measurements*. McGraw-Hill, 264 pp.

Peters, J. M., C. J. Nowotarski, and H. Morrison, 2019: The role of vertical wind shear in modulating maximum supercell updraft velocities. *J. Atmos. Sci.*, **76**, 3169–3189, https://doi.org/10.1175/JAS-D-19-0096.1.

Potvin, C. K., D. Betten, L. J. Wicker, K. L. Elmore, and M. I. Biggerstaff, 2012: 3DVAR versus traditional dual-Doppler wind retrievals of a simulated supercell thunderstorm. *Mon. Wea. Rev.*, **140**, 3487–3494, https://doi.org/10.1175/MWR-D-12-00063.1.

Purser, R. J., W. S. Wu, D. F. Parrish, and N. M. Roberts, 2003: Numerical aspects of the application of recursive filters to variational statistical analysis. Part I: Spatially homogeneous and isotropic Gaussian covariances. *Mon. Wea. Rev.*, **131**, 1524–1535, https://doi.org/10.1175//1520-0493(2003)131<1524:NAOTAO>2.0.CO;2.

Ryzhkov, A. V., M. R. Kumjian, S. M. Ganson, and P. Zhang, 2013: Polarimetric radar characteristics of melting hail. Part II: Practical implications. *J. Appl. Meteor. Climatol.*, **52**, 2871–2886, https://doi.org/10.1175/JAMC-D-13-074.1.

Shapiro, A., K. M. Willingham, and C. K. Potvin, 2010: Spatially variable advection correction of radar data. Part II: Test results. *J. Atmos. Sci.*, **67**, 3457–3470, https://doi.org/10.1175/2010JAS3466.1.

Söder, J., M. Gerding, A. Schneider, A. Dörnbrack, H. Wilms, J. Wagner, and F. J. Lübken, 2019: Evaluation of wake influence on high-resolution balloon-sonde measurements. *Atmos. Meas. Tech.*, **12**, 4191–4210, https://doi.org/10.5194/amt-12-4191-2019.

Son, K., J. Choi, W. P. Jeon, and H. Choi, 2010: Effect of free-stream turbulence on the flow over a sphere. *Phys. Fluids*, **22**, 045101, https://doi.org/10.1063/1.3371804.

Thompson, R. L., R. Edwards, J. A. Hart, K. L. Elmore, and P. Markowski, 2003: Close proximity soundings within supercell environments obtained from the rapid update cycle. *Wea. Forecasting*, **18**, 1243–1261, https://doi.org/10.1175/1520-0434(2003)018<1243:CPSWSE>2.0.CO;2.

Varble, A., and Coauthors, 2014: Evaluation of cloud-resolving and limited area model intercomparison simulations using TWP-ICE observations: 1. Deep convective updraft properties. *J. Geophys. Res.*, **119**, 13 891–13 918, https://doi.org/10.1002/2013JD021372.

Wang, J., J. Bian, W. O. Brown, H. Cole, V. Grubišić, and K. Young, 2009: Vertical air motion from T-REX radiosonde and dropsonde data. *J. Atmos. Oceanic Technol.*, **26**, 928–942, https://doi.org/10.1175/2008JTECHA1240.1.

Waugh, S., and T. J. Schuur, 2018: On the use of radiosondes in freezing precipitation. *J. Atmos. Oceanic Technol.*, **35**, 459–472, https://doi.org/10.1175/JTECH-D-17-0074.1.

Weisman, M. L., and J. B. Klemp, 1982: The dependence of numerically simulated convective storms on vertical wind shear and buoyancy. *Mon. Wea. Rev.*, **110**, 504–520, https://doi.org/10.1175/1520-0493(1982)110<0504:TDONSC>2.0.CO;2.

——, and ——, 1984: The structure and classification of numerically simulated convective storms in directionally varying wind shears. *Mon. Wea. Rev.*, **112**, 2479–2498, https://doi.org/10.1175/1520-0493(1984)112<2479:TSACON>2.0.CO;2.